이학박사 학위논문

Improved Biomeasurement Methods via the Control of Dynamic Flows and Electrical Noises in a Biosensor System

유체흐름 및 전기적 노이즈 제어를 통한 바이오센서 검지능 향상법에 대한 연구

2019 년 2 월

서울대학교 대학원

물리천문학부 물리학 전공

조 동 국

Improved Biomeasurement Methods via the Control of Dynamic Flows and Electrical Noises in a Biosensor System

지도 교수 홍승훈

이 논문을 이학박사 학위논문으로 제출함
2018 년 12 월

서울대학교 대학원
물리천문학부 물리학 전공
조동국

조동국의 이학박사 학위논문을 인준함

2018 년 12 월

위원장 이탁희 (인)
부위원장 홍승훈 (인)
위원 전헌수 (인)
위원 홍성철 (인)
위원 허광 (인)

Improved Biomeasurement Methods via the Control of Dynamic Flows and Electrical Noises in a Biosensor System

by

Dong-guk Cho

Supervised by

Professor Seunghun Hong

A Dissertation Submitted to the Faculty of

Seoul National University

in Partial Fulfillment of the Requirements for the Degree of Doctor of Philosophy

February 2019

Department of Physics and Astronomy

Graduate School

Seoul National University

Abstract

Improved Biomeasurement Methods via the Control of Dynamic Flows and Electrical Noises in a Biosensor System

Dong-guk Cho

Department of Physics and Astronomy

The Graduate School

Seoul National University

Due to increasing demands for early warning systems for harmful virus, air/water pollution and biochemical terrorism, various kinds of bio-sensing systems have been developed. Recently, nano-sized materials adapted in a bio-sensing system enable the system to have high performance which was not available in conventional systems. However, even those advanced bio-sensing systems still show fundamental limitations in their performance such as response speed and sensitivity due to the inherent physical properties of materials. In this dissertation, we discuss about methods to overcome the

fundamental limitations of conventional bio-sensing systems.

First, a high-speed lateral flow strategy to improve the performance of a biosensor by controlling the dynamic flows of a target solution was studied. In this strategy, to create the high-speed lateral flow of the target solution with respect to the biosensor, the biosensor was fixed at a location away from the center of a rotating disk, and the disk was rotated at a rather high speed during the sensing measurement. The lateral flow strategy increased the mass transfer rate of target molecules to the biosensor surface, and the effective collisions between target molecules and receptors on the biosensor surface. Moreover, the lateral flows of a target solution generated weak shear force on the sensor surface. Experimental results show that the lateral flow strategy improved various biosensor performances such as the response speed and sensitivity, the reduction of non-specific bindings. Furthermore, the binding affinity between target and receptors was enhanced even under very harsh environmental conditions such as an acidic pH and a low ionic concentration. These results clearly show that the performance of conventional biosensors could be improved simply by moving the sample solution laterally with a high speed.

Next, we studied electrical noises in bio-sensing materials in order to improve the performance of a bio-sensing system. In this study,

electrical noise analysis was carried out with respect to PEDOT: PSS conducting polymer via a scanning noise microscopy (SNM) system. Using the SNM system, we can obtain current and electrical noise maps with a nanometer resolution. The experimental results show that the noise sources which were charge trap sites were non-uniformly distributed in the PEDOT:PSS film, and the density of the noise sources showed the anomalous switching behaviors according to the external applied voltage. Moreover, the anomalous switching behaviors were strongly related with the electrical characteristics of the PEDOT:PSS film. This study shows that there are optimal experimental conditions to minimize electrical noises in a PEDOT:PSS film, and those conditions could be applied in PEDOT:PSS based biosensing device for lowering the detection limit of the device.

Keywords: Biosensor, Lateral flows, Binding affinity, Non-specific bindings, Scanning noise microscopy, Electrical noise, Charge trap
Student Number: 2012-30109

Table of contents

List of figures

Chapter 1

Introduction

1.1 Biosensing System

Bio-sensing systems are commonly referred to as a system that transform biological or chemical reactions into a signal that can be recognized by humans. The systems are employed in many applications such as harmful pathogen detection, drug monitoring, water pollution inspection, and the prevention of bio-terrorism [1-4].

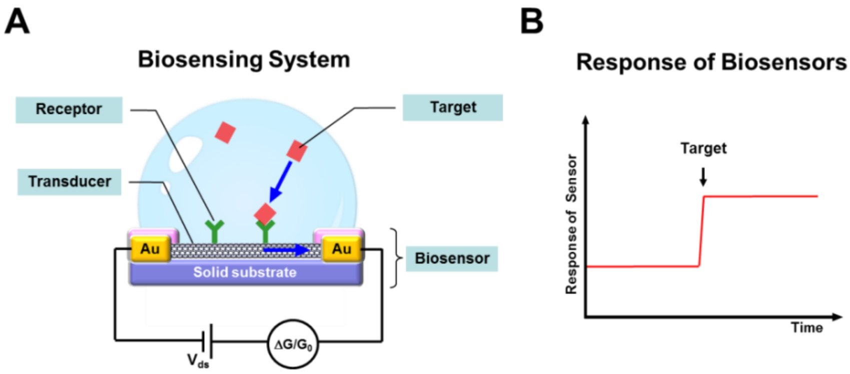

Figure 1-1. (A) Schematic diagram of a bio-sensing system (B) the example of the sensing response of a biosensor

A typical bio-sensing system is represented in figure 1-1A. The bio-sensing system consists of target, receptor and transducer, and the system operates by interactions between the components. Briefly, a receptor which can selectively capture target molecules is fixed to the transducer of a biosensor, and when the target molecules are captured by the receptor, the physical properties of the transducer are changed.

The changed physical quantities of the transducer are converted into optical or electrical signals by the system to display the detection of target molecules (Figure 1-1B).

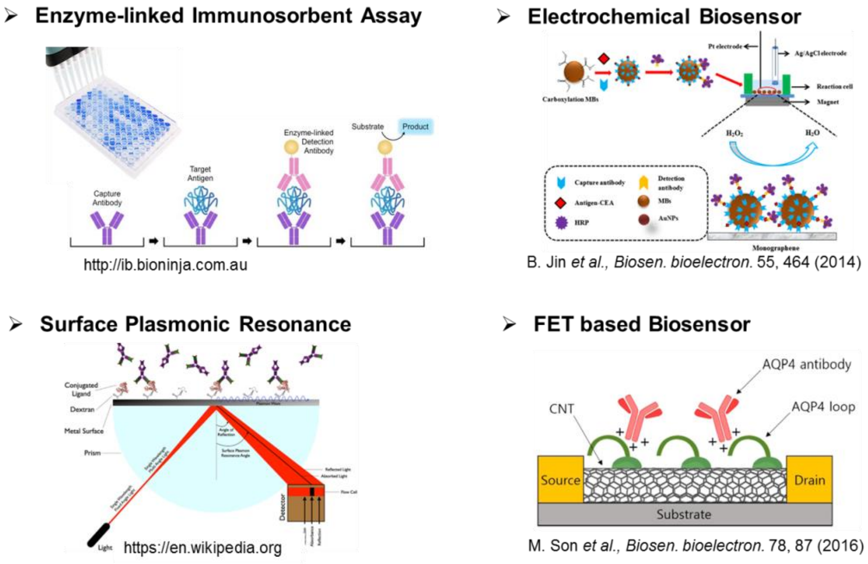
➢ **Enzyme-linked Immunosorbent Assay**

http://ib.bioninja.com.au

➢ **Electrochemical Biosensor**

B. Jin *et al.*, *Biosen. bioelectron.* 55, 464 (2014)

➢ **Surface Plasmonic Resonance**

https://en.wikipedia.org

➢ **FET based Biosensor**

M. Son *et al.*, *Biosen. bioelectron.* 78, 87 (2016)

Figure 1-2. Schematic diagram depicting conventional bio-sensing systems

In the past, enzyme-linked immunosorbent assays were commonly utilized to detect hazardous biomolecules such as bacteria, fungi and virus [5-7] (Figure 1-2), but there were some shortcomings to limit their utilization. Specifically, it involves multi-step processing, well-trained personnel and considerable time. Recently, surface plasmonic resonance (SPR) and field effect transistor (FET) based techniques which do not require a complicated step have been developed [2, 8]. These techniques showed excellent sensing characteristics such as fast detection speed and low detection limit. However, they required expensive equipment and had a fundamental limitation in performance due to electrical noises from the equipment.

1.2 Conventional Methods for High Performance Bio-sensing Systems

Although there have been many advances in bio-sensing systems in the last few decades, many improvements are still needed in the response speed, sensitivity, and accuracy of the system. In particular, most bio-sensing systems have fundamental problems due to their biological or physical limitations, thus, addressing these issues is essential for developing biosensors with improved performance.

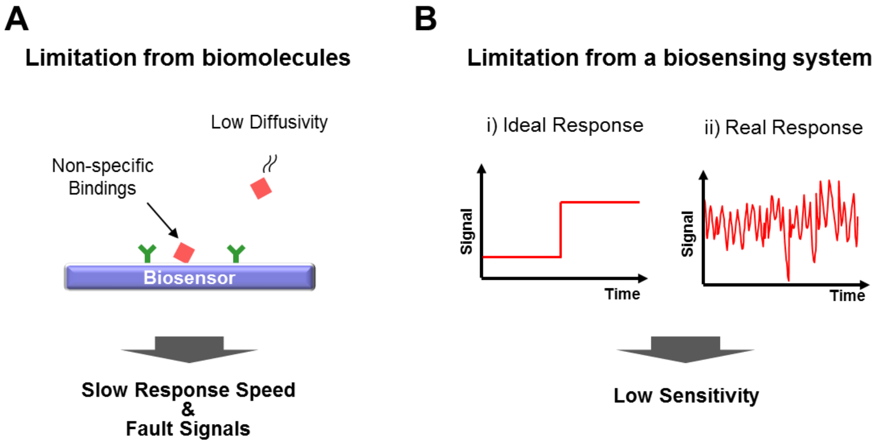

Figure 1-3. Limitation of a conventional bio-sensing system (A) Limitation from biomolecules (B) Limitation from a bio-sensing system

Figure 1-3 shows the several factors which limit the performances of bio-sensing systems. For example, the diffusivity of the target molecules affect the detection limit and speed of a biosensor [9]. Moreover, the non-specific binding of molecules could lead to a decrease in the sensitivity of biosensors by increasing background noises in sensor signals [10] (Figure 1-3 A). Moreover, the electrical noises of a bio-sensing system often excess the response signals of target detections, which limit the sensitive target detection of the system (Figure 1-3 B).

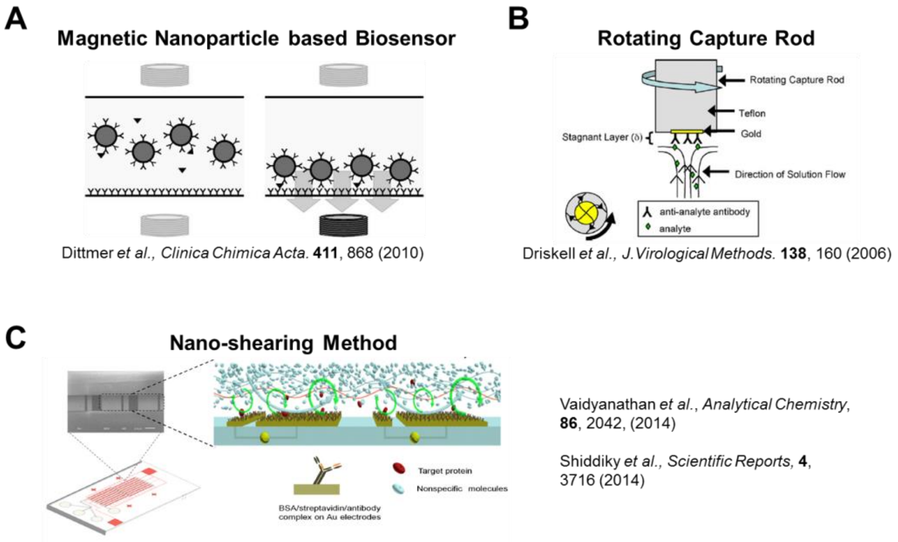

Magnetic Nanoparticle based Biosensor

Dittmer *et al.*, *Clinica Chimica Acta.* **411**, 868 (2010)

Rotating Capture Rod

Driskell *et al.*, *J. Virological Methods.* **138**, 160 (2006)

Nano-shearing Method

Vaidyanathan *et al.*, *Analytical Chemistry*, **86**, 2042, (2014)

Shiddiky *et al.*, *Scientific Reports*, **4**, 3716 (2014)

Figure 1-4. Various approaches to enhance the performance of bio-sensing systems (A) Magnetic nanoparticle based biosensor (B) Rotating capture rod system (C) Nano-shearing method

Recently, various techniques have been suggested to overcome the fundamental limitations of bio-sensing systems. Figure 1-4 shows various approaches to enhance the performance of bio-sensing systems. An active bio-sensing strategy using magnetic particles was used for enhancing the detection speeds of biosensors, where target molecules were captured by the magnetic particles and delivered to the sensing part of the bio-sensing system [11] (Figure 1-4A). A rotating disk system has been also developed to overcome the detection speed limit of conventional biosensor systems [4, 12, 13] (Figure 1-4 B). In this case, sensors are fixed at the center of a rotating disk and rotated at a high speed. The rotation of the disk could increase the vertical influx of target molecules toward the sensor surface. These methods can be utilized to improve detection speed, but it is difficult to enhance the sensitivity and selectivity of a biosensor. As another example of advanced bio-sensing system, the lateral fluid flows of an analyte solution have been utilized to enhance the selectivity of a biosensor by removing nonspecifically bound molecules from the capture surface of a biosensor [14, 15] (Figure 1-4 C). In this method, alternating current (AC) electric fields are utilized to drive the lateral fluid flows of the analyte solution on the sensor surface. However, this method requires a specifically patterned structure of the biosensor and precise control of the AC electric fields in order to generate lateral flows on the sensor, which makes it expensive and tricky.

Addressing noise signals in a bio-sensing system are also good approaches to develop high performance bio-sensing systems. Recently, some studies reported the improved performance of a bio-sensing system by removing the electrical noise signals of sensors [16], which directly showed the importance of eliminating the electrical noise signals in a sensor performance. Meanwhile, recently developed biosensors tend to use nano-sized materials such as carbon nano tube, graphene and conducting polymers [2, 17, 18]. However, there was little progress in the study of noise analysis with a nano-scale resolution for these nano-sized materials. Therefore, by studying noise signals in the nano-sized materials, we can expect the improved bio-sing system with high speed, sensitivity and accuracy.

1.3 References

[1] Park K. T.; Cho D. G.; Park J. W.; Hong S.; Hwang J., *Scientific Reports*, **2015**, 5.

[2] Ba V. A. P.; Cho D. G.; Kim D.; Yoo H.; Ta V. T.; Hong S., *Biosensors & Bioelectronics*, **2017**, 94, 707-713.

[3] Son M.; Cho D. G.; Lim J. H.; Park J.; Hong S.; Ko H. J.; Park T. H., *Biosensors & Bioelectronics*, **2015**, 74, 199-206.

[4] Driskell J. D.; Uhlenkamp J. M.; Lipert R. J.; Porter M. D., *Analytical Chemistry*, **2007**, 79, 4141-4148.

[5] Ferguson C. M. J.; Booth N. A.; Allan E. J., *Letters in Applied Microbiology*, **2000**, 31, 390-394.

[6] Zahradnik E.; Kespohl S.; Sander I.; Schies U.; Khosravie-Hohn J.; Lorenz W.; Engelhart S.; Kolk A.; Schneider G.; Bruning T.; Raulf-Heimsoth M., *Environmental Science-Processes & Impacts*, **2013**, 15, 1162-1171.

[7] Edwards M. L.; Cooper J. I., *Journal of Virological Methods*, **1985**, 11, 309-319.

[8] Baumgarten S.; Robelek R., *Sensors and Actuators B-Chemical*, **2011**, 156, 798-804.

[9] Nair P. R.; Alam M. A., *Nano Letters*, **2008**, 8, 1281-1285.

[10] Myszyka D. G., *Journal of Molecular Recognition*, **1999**, 12, 279-284.

[11] Dittmer W. U.; Evers T. H.; Hardeman W. M.; Huijnen W.; Kamps R.;

de Kievit P.; Neijzen J. H. M.; Nieuwenhuis J. H.; Sijbers M. J. J.; Dekkers D. W. C.; Hefti M. H.; Martens M. F. W. C., *Clinica Chimica Acta*, **2010**, 411, 868-873.

[12] Driskell J. D.; Kwarta K. M.; Lipert R. J.; Vorwald A.; Neill J. D.; Ridpath J. F.; Porter M. D., *Journal of Virological Methods*, **2006**, 138, 160-169.

[13] Wang G. F.; Driskell J. D.; Hill A. A.; Dufek E. J.; Lipert R. J.; Porter M. D., *Annual Review of Analytical Chemistry, Vol 3*, **2010**, 3, 387-407.

[14] Shiddiky M. J. A.; Vaidyanathan R.; Rauf S.; Tay Z.; Trau M., *Scientific Reports*, **2014**, 4.

[15] Vaidyanathan R.; van Leeuwen L. M.; Rauf S.; Shiddiky M. J. A.; Trau M., *Scientific Reports*, **2015**, 5.

[16] Karandikar N.; Jung S.; Sun Y. Z.; Chung H. J., *Analog Integrated Circuits and Signal Processing*, **2016**, 89, 417-424.

[17] Justino C. I. L.; Comes A. R.; Freitas A. C.; Duarte A. C.; Rocha-Santos T. A. P., *Trac-Trends in Analytical Chemistry*, **2017**, 91, 53-66.

[18] Aydemir N.; Malmstrom J.; Travas-Sejdic J., *Physical Chemistry Chemical Physics*, **2016**, 18, 8264-8277.

Chapter 2

Lateral Flow Strategy for a Fast Bio-sensing with High Selectivity and Binding Affinity

2.1 Lateral Flow Strategy

As we discussed in the introduction section, most of a bio-sensing system have the fundamental limitations in their functions. In this chapter, a dynamical strategy which controls the fluid flows of a target solution is discussed to solve the fundamental limitation of a bio-sensing system.

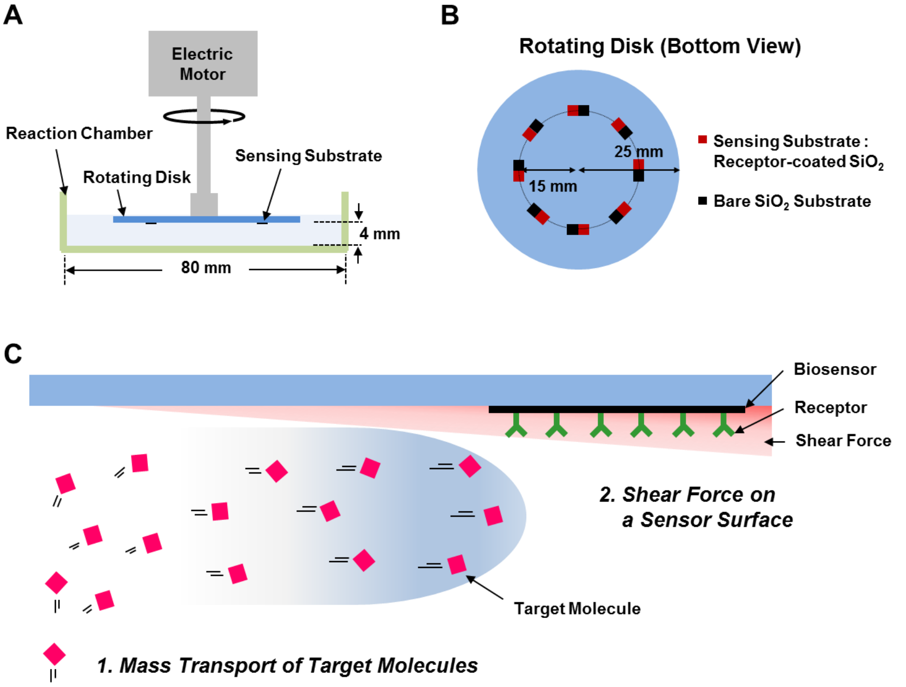

Figure 2-1. Schematic diagram of a lateral flow strategy (A) High-speed lateral flow system (B) A rotating disk with bio-sensing substrates (C) The motion of target molecules near the surface of a bio-sensing substrate

Figure 2-1A shows the schematic diagram of a high-speed lateral flow bio-sensing system. The system was consisted of a reaction chamber and a rotating disk which was connected to an electrical motor via a rotating bar. The reaction chamber containing a target solution was a commercial petri dish with a diameter of 80 mm. The rotating disk had a dimeter of 25 mm, and biosensors and bare SiO_2 substrates were attached on the disk side by side at 15 mm regions from the center of the disk (Figure 2-1B). A distance between the rotating disk and the bottom of the reaction chamber was 4 mm. The system was designed to generate the high-speed lateral flows of a target solution on the biosensors and bare SiO_2 substrates, when the disk was rotated in the target solution. The lateral flow speed of the target solution was simply calculated by multiplying the angular velocity of the rotating disk by a distance from the center of the disk to the position of the biosensor.

Figure 2-1C shows the plausible motions of target proteins near the surface of biosensors under a lateral flow condition. When a rotating disk containing the biosensors is rotated in a target solution, the convective flows of the target solution are generated in a reaction chamber. The convective flows deliver the target molecules continuously to the biosensor surface, which could enhance the mass transfer rate of target molecules to the biosensor surface. Moreover the lateral flows generate a weak shear force on the biosensor surface, which may remove weakly bound molecules on the biosensor surface. Since the diffusivity of target molecules and the non-specific bindings of molecules cause problems in the performance of biosensor systems, the high-speed lateral flow system could improve the performance of biosensors.

2.2 Experimental Method

Figure 2-2 shows the experimental procedures with a high-speed flow system. As a proof of concept, we used a receptor-coated SiO_2 substrate as a biosensor considering the sensing part of conventional biosensors. Because conventional biosensors used a receptor-coated surface for capturing target molecules, the receptor-coated SiO_2 substrates were chosen as a simple biosensor in the system. Specifically, we used biotin-coated SiO_2 substrates for detecting streptavidin proteins and interleukin-13 (IL-13) antibody-coated SiO_2 substrates for detecting IL-13 antigen proteins. Fluorescence assay and enzyme linked immunosorbent assay (ELISA) were used to detect streptavidin molecules and IL-13 antigens, respectively. Bare SiO_2 substrates were used for analyzing the non-specific bindings of target proteins. Since the system can easily generate the lateral flows of a target solution just by the arrangement of biosensor positions on a rotating disk, it could be utilized in various bio-sensing systems.

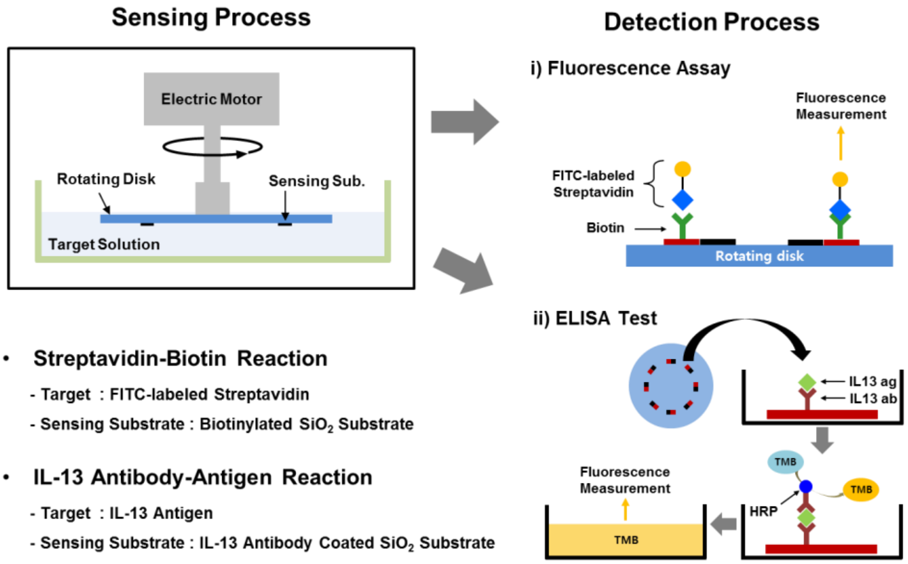

Figure 2-2. Experimental procedures with a high-speed lateral flow system. The experiments were performed with i) fluorescence assay and ii) enzyme-linked immunosorbent assay (ELISA)

2.2.1. Test on fluorescence assay

Our lateral flow bio-sensing system was tested on fluorescence assay. Streptavidin molecules labeled with fluorescein isothiocyanate dyes (FITC-labeled streptavidin) and biotinylated SiO_2 substrates were utilized as target molecules and biosensors, respectively. The biotinylated SiO_2 substrates were prepared using a biotinylation method reported previously [19]. Briefly, cleaned SiO_2 substrates (3 mm x 3 mm) were immersed in an 3-aminopropyl-triethoxysilane (APTES, Sigma aldrich, 440140) solution (APTES : toluene = 1 : 100) at 70 ℃ for 12 hours. The APTES coated substrates were transferred to a 2 mg/ml biotin N-hydroxysuccinimide ester (biotin-NHS, Sigma Aldrich, H1759) solution for 1 hour at a room temperature for the biotinylation of biotin-NHS molecules with APTES molecules on the substrates. Then, the biotinylated substrates were washed three times with a phosphate buffered saline (PBS) solution to remove loosely-bound biotin-NHS molecules on the substrates. For blocking nonspecific binding sites, the substrates were incubated in a 2 wt % bovine serum albumin (BSA, Sigma Aldrich, A2153) solution for 1 hour, and then the prepared biotinylated substrates were fixed on a rotating disk using double-sided adhesive tapes. Next, we prepared 1 ng/ml streptavidin target solutions by dissolving FITC-labeled streptavidin powders (Sigma Aldrich, S3762) in 2 wt % BSA-diluted PBS solution. For the sensing experiments of streptavidin molecules, the rotating disk including the biotinylated substrates was immersed in the target solution, and the disk was rotated to generate the static and lateral flow of the target solution for 90 min. The rotating speeds of the disk were adjusted to achieve the desired lateral flow speeds of the target solution on the biotinylated substrates (0 mm/s for static conditions and 110 mm/s for lateral flow conditions). After the sensing procedures, the disk was gently washed three times with a PBS solution, and the fluorescence intensities of the biotinylated substrates were measured by a fluorescence microscope (Eclipse te2000-u, Nikon) in a PBS solution. All experiments were repeated at least three times with eight samples in each experiment.

2.2.2. Test on ELISA

We also tested our method on conventional enzyme-linked immunosorbent assay (ELISA) using commercial ELISA test kits (Ready-Set-Go!, IL-13 ELISA test kit from eBioscience). First, IL-13 antibodies were coated on SiO_2 substrates using a previous protein coating method [20]. Briefly, cleaned SiO_2 substrates were immersed in a 3-Mercaptopropyl trimethoxysilane (MTS, Sigma Aldrich, 175617) solution (MTS : toluene = 1 : 50) at room temperature for 2 hours. The substrates were rinsed by toluene and dried with the stream of nitrogen gases. Then, the MTS coated substrates were immersed in a 4-Maleimidobutyric acid N-hydroxysuccinimide ester (GMBS, Sigma Aldrich, 63175) solution (2 mM GMBS in DI water) for 2 hours at a room temperature, and the substrates were washed three times with DI water. The GMBS coated substrates were transferred to a 96 well plate, and the substrate were incubated with the 100 ul/well of IL-13 antibody solutions for 12 hours at 4℃. These IL-13 antibody-coated substrates were used as biosensors for capturing IL-13 antigens. The substrates were fixed onto a rotating disk using double-sided adhesive tapes. Next, the target solutions of IL-13 antigens were prepared in 2 wt% BSA solutions with concentration ranges from 0.01 to 100 ng/ml. For the sensing procedures of IL-13 antigens, the rotating disk including the the IL-13 antibody-coated substrates was immersed in IL-13 antigen solutions for 2 hours under static and lateral flow conditions. After the sensing procedures, the reacted substrates were collected from the disk and were placed in a new 96 well plate for the remaining steps of ELISA. For forming the sandwich structures of the 1st antibody-antigen-2nd antibody, the substrates were incubated in 100 uL of biotin-linked 2nd antibody solutions for 1 hour at room temperature followed by 5 times of rinsing with a wash buffer (1x PBS with 0.05 % Tween-20). Then, the substrates were treated with avidin-linked horseradish peroxidase (HRP) solution and tetramethylbenzidine (TMB) solution for 30 min and 15 min, respectively. Then, 1 M H_3PO_4 solutions were applied to stop the enzyme reactions of HRP with TMB. Reacted solutions were transferred to a new 96 well plate. Finally, the absorbance values of the transferred solutions were measured using a multiple plate reader (Victor3, USA, Perkin Elmer) at 450 nm.

2.2.3. Simulation

A commercial finite element method package (COMSOL Multiphysics) was used for the simulation of fluidic flows and shear rates in a reaction chamber. A two-dimensional cross section structure including a rotating disk, a target solution and a reaction chamber was considered for the simulation. A rotational symmetric boundary condition was applied. Three modules of a laminar flow interface, a transport interface and a reaction interface were utilized. We applied Reynolds-averaged Navier-Stokes (RANS) model for the simulation of dynamic flows in a reaction chamber with incompressible fluid condition. Wall function boundary condition was used for the reaction chamber, and the rotating disk was considered as a sliding wall. To calculate the shear force of a target solution for bound target molecules at the 15 mm region of the disk, we attached a 10 nm-sized particle on the region and simulated the shear rate of the solution. The shear force near the particle was estimated by multiplying the shear rate with the viscosity of the solution.

2.3 Response Speed

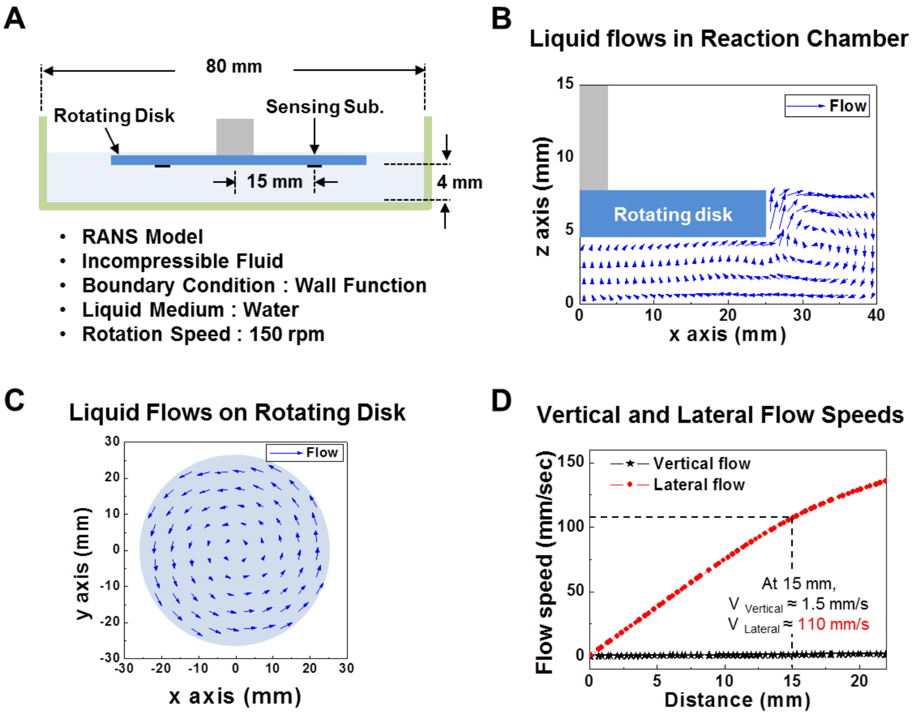

Figure 2-3. Simulation results of the fluid flows of a target solution. (A) Experimental conditions for simulations (B) Simulated flows of a target solution in a reaction chamber (C) Simulated flows on a rotating disk (D) Vertical and lateral flow speeds as a function of a distance from the center of the disk

Figure 2-3A shows the schematic diagram of a rotating disk system and conditions for a computational fluid simulation. The rotating disk had a dimeter of 25 mm, and biosensors and bare SiO_2 substrates were attached on the disk side by side at 15 mm regions from the center of the disk. A distance between the rotating disk and the bottom of the reaction chamber was 4 mm. We assumed water as a target solution, and 1 mPa·s of a viscosity was used for simulation. The rotating disk was rotated with 150 rpm. The convective flows of the target solution were simulated without turbulent flows in a reaction chamber (Figure 2-3B), and the speed of lateral flows increased as the distance from the center of the disk increase (Figure 2-3C). We also simulated cell Reynolds numbers for turbulent estimation in the system, and include in Appendix section. We plotted the vertical and lateral flow speeds along the distance (Figure 2-3D), and found that the lateral flow speeds were proportional to the distances from the center of the disk, while the vertical flow speeds remained almost unchanged. The simulated lateral flow speed of the target solution at 15 mm was 110 mm/s. For the precise simulation of flow dynamics in our system, we also simulated the system including sensing substrates and showed it in Appendix section in this dissertation.

Figure 2-4A shows the fluorescence image of a bare SiO_2 substrate (left) and a biotinylated SiO_2 substrate (right) after reactions with FITC-labeled streptavidin molecules under a static condition. The reactions were conducted for 90 min, and then the fluorescence images of both substrates were obtained in a PBS solution by a fluorescence microscope. The biotinylated substrate exhibited much brighter fluorescence intensities than the bare SiO_2 substrate. Since fluorescence intensities are correlated with the amount of bound FITC-labeled streptavidin molecules on the biotinylated substrates, the results indicate that the biotinylated substrate could selectively capture streptavidin molecules.

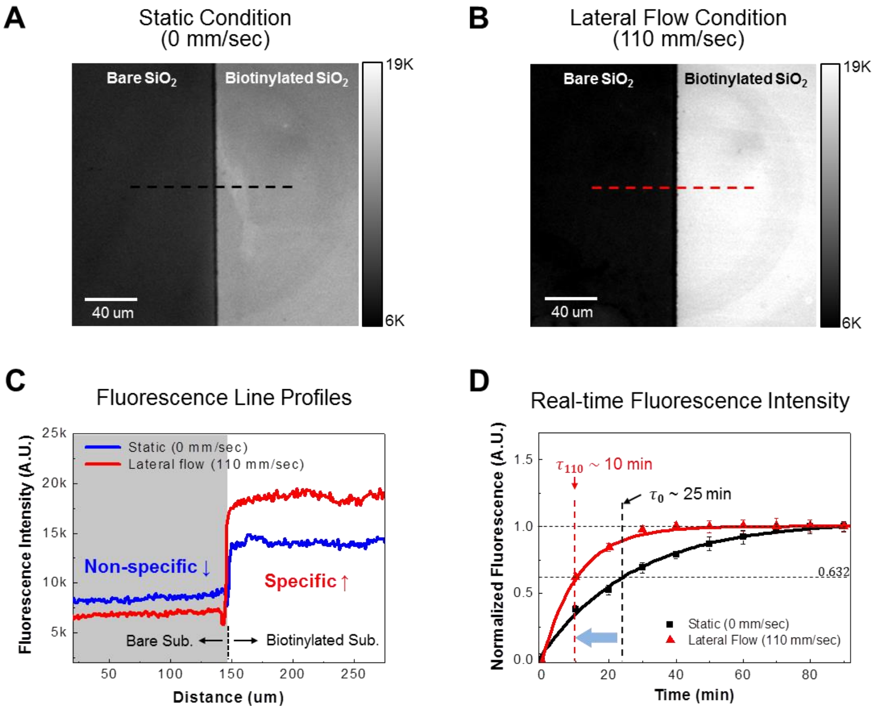

Figure 2-4. Effect of lateral flows on binding reactions between a biotinylated SiO_2 substrate and streptavidin molecules (A) Fluorescence images of bare and biotinylated SiO_2 substrates after reactions with FITC-labeled streptavidin molecules under a static condition (B) Fluorescence images of bare and biotinylated SiO_2 substrates after reactions with FITC-labeled streptavidin molecules under a lateral flow condition (C) Comparison of amount of bound streptavidin molecules on a bare and a biotinylated SiO_2 substrates with or

without lateral flows (110 mm/s). The fluorescence profiles were obtained from the fluorescence images of figure 1A and 1B. (D) Real time fluorescence measurements on biotinylated SiO_2 substrates under static and lateral flow conditions

We also conducted a reaction experiment under a lateral flow condition. Figure 2-4B shows the fluorescence image of bare and biotinylated SiO_2 substrates after reactions with streptavidin molecules for 90 min. In the experiment, we fixed the biotinylated substrates at 15 mm away from the center of a rotating disk, and the disk was rotated 150 rpm to achieve the lateral flow speed ~110 mm/s of a target solution of on the biotinylated substrate. Note that, the biotinylated substrate under the lateral flow condition exhibited higher fluorescence intensities than that under the static condition. It indicates that the lateral flows of target solutions could increase the binding events between target molecules and their receptors on a substrate.

Figure 2-4C shows the fluorescence intensity profiles of the bare and the biotinylated SiO_2 substrates under static (red line) and lateral (black line) flow conditions. The profiles were obtained along a black-dotted line in figure 2-4A and a red-dotted line in figure 2-4B. The average fluorescence intensities of the biotinylated substrate are about 14,100 under the static condition and about 18,570 under the lateral flow condition. These results indicate the 31.7 % increase of bound streptavidin molecules on the biotinylated substrate simply by flowing the target solution laterally. Interestingly, the average fluorescence intensities of the bare SiO_2 substrates are ~8,440 under the static condition and ~6,860 under the lateral flow condition, which indicates the 18.7 % decrease of bound target molecules by the lateral flows of a target solution on the bare SiO_2 substrates. These results indicate that the lateral flow of target solution can not only increase the specific bindings (SB) on the biotinylated substrate but also decreased the nonspecific bindings (NSB) on the bare SiO_2 surface.

Figure 2-4D shows the real-time fluorescence measurement data obtained from biotinylated SiO_2 substrates during reactions with FITC fluorescent-labeled streptavidin molecules under static and lateral flow conditions. To evaluate the sensing speed, the data were fitted by the first order rate equation [21] like

$$A(t) = A_{max}[1 - e^{-\frac{t}{\tau}}] \tag{1}$$

where, $A(t)$, A_{max}, and τ indicate the amount of bound target molecules on a biosensor at time t, the maximum amount of bound target molecules on the biosensor, and the characteristic time constant of the reaction, respectively. By fitting the data we could estimate the time constants τ of the biotinylated substrates under static and lateral flow condition as ~ 25 min and ~ 10 min, respectively. Note that, the time constant of the substrates under the lateral flow condition was reduced by 60% compared with that of the substrates under the static condition. The enhancement of a response speed under a lateral flow condition can be explained by the increase of mass transfer rate of target molecules to a sensor surface. Previously, it was reported that the accumulation of bound target molecules, represented by its surface concentration Γ, on a sensor surface is dependent on the rotational rate ω of a rotating disk [4].

$$\Gamma(t) = \frac{2}{\pi^{\frac{1}{2}}} D^{\frac{1}{2}} C_b t^{\frac{1}{2}} + \frac{D^{\frac{2}{3}} C_b}{1.61 v^{\frac{1}{6}}} t \omega^{\frac{1}{2}} \tag{2}$$

where D is the antigen diffusion coefficient, C_b is the bulk concentration of antigen, t is the incubation time, v is the kinematic viscosity of the solution. The first term on the right-hand side of the equation (2) represents the contribution of diffusional mass transfer, whereas the second term defines the additional mass transfer of target molecules due to the rotation of the disk. The rotation continuously generates convective flows in a reaction chamber, which increase the mass transfer of target molecules. Therefore, the lateral flow of target solutions generated by the rotation of a disk can significantly increase the response speed of a sensing substrate.

2.4 Binding Affinity

Figure 2-5A shows the fluorescence images of bare and biotinylated substrates i) before reactions with FITC-labeled streptavidin molecules, ii) after the reactions under a static condition for 90 min and iii) after the reactions under static and lateral flow condition for 170 min. The reaction experiments were sequentially performed under a static condition for 90 min, and then under a lateral flow condition for 80 min. Before reactions with FITC-labeled streptavidin molecules (Figure 2-5A i)), only background fluorescence intensities were measured on the both bare and the biotinylated substrates. After the reactions under the static condition (Figure 2-5A ii)), clear differences in fluorescence intensities between bare and biotinylated substrates were observed. Interestingly, after the reactions under the lateral flow condition (Figure 2-5A iii)), fluorescence intensities of the biotinylated substrate increased, while fluorescence intensities of the bare SiO_2 substrate slightly decreased compared to those of a bare SiO_2 substrate in figure 2-5A ii).

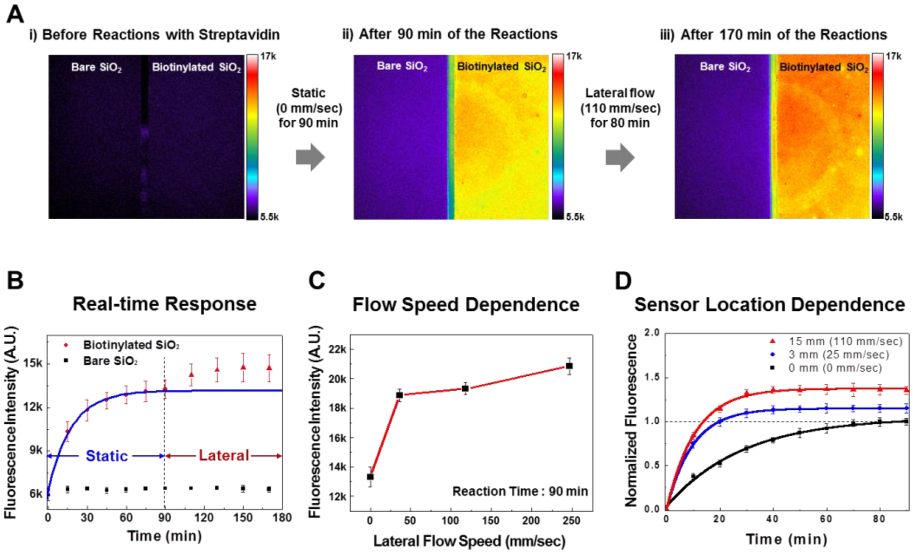

Figure 2-5. (A) i) Fluorescence image of bare and biotinylated substrates before reactions with FITC-labeled streptavidin molecules, ii) Fluorescence image of both substrates after 90 min of the reactions under a static condition, iii) Fluorescence image of both substrates after 170 min of the reactions under static and lateral flow conditions. The experiment was performed under static condition for 90 min, followed by under a lateral flow condition for 80 min. (B) Real time response curves of bare (black square) and biotinylated (red triangle) substrates to FITC-labeled streptavidin molecules. The experiments were conducted under same conditions of figure 4A. (C) Lateral flow speed dependence in sensing response. (D) Real-time fluorescence measurement on biotinylated substrates with different position. The biotinylated substrates were fixed to a rotating disk at 0, 3 and 15 mm from the center of the disk.

The results show that the lateral flow increases specific binding reactions between streptavidin and biotin molecules while decreasing the nonspecific bindings of streptavidin molecules. These results are consistent with the results of figure 2-4A and 2-4B indicating the reliability of our observations.

Figure 2-5B shows the real-time response curves of bare (black square) and biotinylated (red triangle) substrates during reactions with FITC-labeled streptavidin molecules. Here, the same experimental conditions with the experiments of figure 2-5A were used for real-time response experiments. The experimental data of biotinylated substrates under static conditions were fitted by the equation (1), and the fitted curve was marked in a blue line. Black dot in the figure represent the fluorescence intensities of bare SiO_2 substrates, which indicate the amount of the nonspecific adsorptions of streptavidin molecules. The specifically bound streptavidin molecules to the biotinylated substrates were almost saturated in 90 min under the static condition and increased again when we applied the lateral flows on the substrates. Note that, the fluorescence intensities of bare SiO_2 substrates showed negligible changes by the lateral flow. This result indicates that the enhanced binding reactions like those between streptavidin and biotin molecules under lateral flow conditions did not increase the nonspecific adsorptions of streptavidin molecules.

Figure 2-5C shows the lateral flow speed dependence in sensing response. We changed the lateral flow speed by increasing the rotation speed of the rotating disk. The results show the increase of fluorescence intensities as lateral flow speed increase. However, the increasing rate of fluorescence intensity was rather higher in the low flow speed than high flow speed. This result indicates that the binding reaction could increase even with low speed lateral flows.

Figure 2-5D shows the real-time fluorescence measurement data obtained from biotinylated SiO_2 substrates during reactions with FITC fluorescent-labeled streptavidin molecules. In this experiment, the biotinylated substrates were fixed at 0, 3 and 15 mm from the center of the disk, and the disk was rotated with 150 rpm to achieve the lateral flow of the target solution with the speeds of 0, 25 and 110 mm/s, respectively. After the 90 min reactions, the fluorescence intensities of the biotinylated substrates at 0, 3 and 15 mm from the disk center were reached 0.632, 1.064 and 1.246, respectively. Note that the substrates with a larger lateral flow exhibited a larger binding of target molecules even with the same reaction time, indicating enhanced binding events of target molecules by lateral solution flow. These results imply that the binding events between a biotinylated substrate and its target molecules are strongly affected by the lateral flow of target molecules.

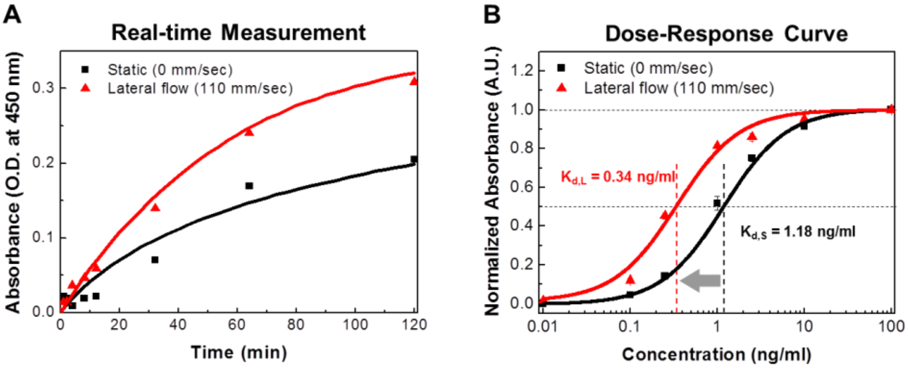

Figure 2-6. Effects of lateral flow conditions on IL-13 antibody-antigen reactions: (A) Absorbance values of bound IL-13 antigens to IL-13 antibody-coated substrates with or without lateral flows (110 mm/s); (B) Dose-response of IL-13 antibody-coated substrates to IL-13 antigens with or without lateral flows (110 mm/s).

To confirm the enhanced binding kinetics by a lateral flow system in an immune system, we performed a binding reaction test using a commercial ELISA test kit which includes IL-13 antibody-antigen immune proteins. More detail procedures were written in 2.2 Experimental Method section in this article. Figure 2-6A shows the absorbance values of bound IL-13 antigens to IL-13 antibody-coated substrate under static (black dot) and lateral (red dot) flow conditions. We loaded eight IL-13 antibody-coated substrates on a rotating disk and performed reaction experiments in IL-13 antigen target solution with or without lateral flows (110 mm/s). During the reaction process, each reacted substrate was collected from the disk in accordance with reaction time, and the absorbance values of the reacted substrates were obtained by using an ELISA method. The absorbance data points were fitted by the equation (1). The graph shows that the responses under the lateral flow condition exhibited higher absorbance values than those under the static condition. Since absorbance values indicate the amount of bound IL-13 antigens to the antibody-coated substrates, the results show that the amount of bound IL-13 antigens increased by the lateral flows of the target solution even in an immune protein reaction. Through the results, we could expect that the lateral flow strategy can be applied in various sensing applications simply by changing sensing substrates from a rotating disk.

Figure 2-6B shows the dose-response of IL-13 antibody-coated substrates to IL-13 antigens under static and lateral flow conditions. The reaction experiments were conducted in IL-13 antigen solution for 2 hours with the concentration range of the IL-13 antigen solution from 0.01 to 100 ng/ml. The experimental data points were fitted by a Hill's equation [22]. Under the static conditions, the equilibrium dissociation constant K of IL-13 was about 1.18 ± 0.1 ng/ml, which was consistent with previously reported value [23]. However, under the lateral flow conditions, the constant K of IL-13 was about 0.34 ± 0.08 ng/ml, which is three times lower than that under the static condition. It indicates an enhanced binding affinity in an immune protein reaction by the lateral flow of a target solution, which has not been reported before. We also estimated the limit of detection (LOD) from the figure 2-6B. The limit of detection is defined as the concentration yielding a signal equal to the blank signal plus three times its standard deviation [13, 24]. Based on the results of IL-13 tests, LOD was obtained as 69 ± 1 pg/ml and 21 ± 0.3 pg/ml under static and lateral flow conditions, respectively. These results clearly show the enhanced LOD under the lateral flow condition.

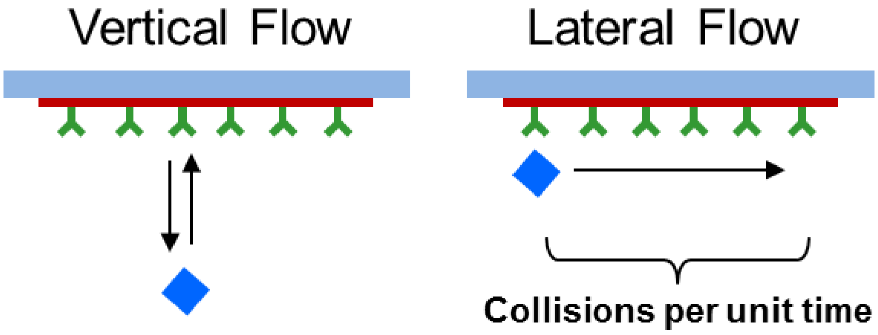

Figure 2-7. Schematic diagram depicting the flow direction of a target molecule under vertical and lateral flow conditions

The enhancement of binding affinity between target and receptor-coated sensing substrates under a lateral flow condition could be explained by a collision between target and receptors. A general reaction between A and B can be written like,

$$A \quad + \quad B \quad \underset{k_{on}}{\overset{k_{off}}{\overleftarrow{\underrightarrow{\quad\quad}}}} \quad AB \tag{3}$$

where k_{on} and k_{off} are on-rate and off-rate constant, respectively. The equilibrium dissociation constant of the reaction are determined as follows

$$K_d = \frac{[A][B]}{[AB]} = \frac{k_{off}}{k_{on}} \tag{4}$$

Here, the increase of k_{on} leads to the decrease of K_d, which indicates the increase of total concentration of complex AB in their equilibrium state. Moreover, the k_{on} is affected by collisions between reactant A and B [25].

$$k_{on} = Z\,exp\left[\frac{-\Delta G}{kT}\right] \tag{5}$$

where Z, ΔG, k and T are a collision frequency, the Gibbs free energy of activation, Boltzmann constant and absolute temperature T. Figure 2-7 shows a schematic diagram depicting the flow direction of a target molecule under vertical and lateral flow conditions. Compared with a collision rate between target and receptors in the case of the vertical motion of a target molecule, the lateral motion of a target molecule could increase the collision rate in a unit time, which results in the increase of k_{on} in the molecular reaction. Therefore, the K_d value decrease and an binding affinity between target and receptor increase.

2.5 Non-specific Bindings

Figure 2-8A shows the nonspecific binding reaction curves of FITC-labeled streptavidin molecules to bare SiO_2 substrates under static and lateral flow conditions. To obtain only nonspecifically bound streptavidin molecules, bare SiO_2 substrates were reacted with FITC-labeled streptavidin molecules with or without lateral flows (110 mm/s) for 90 min. Black square and red triangle in the graph indicate experimental data under static and lateral flow conditions, respectively. The graph shows the fluorescence intensities of bare SiO_2 substrates reacted with FITC-labeled streptavidin molecules under static conditions increase as reaction time increase. On the other hand, under lateral flow conditions, the fluorescence intensities of a bare SiO_2 substrate reacted with FITC-labeled streptavidin molecules rapidly increase during 40 min. Then the fluorescence intensities are saturated. The saturated intensities are lower than the fluorescence intensities under static conditions. It implies that the lateral flows of a target solution hinder the nonspecific adsorptions of streptavidin molecules.

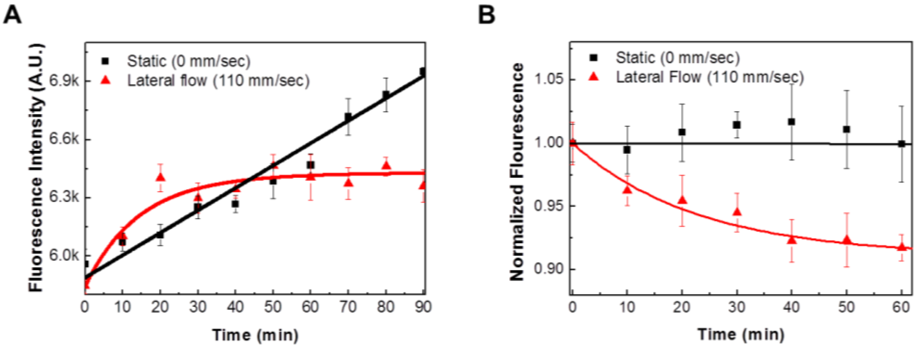

Figure 2-8. (A) Nonspecific binding reaction curves of streptavidin molecules to bare SiO_2 substrates under static and lateral flow conditions (B) Dissociation curves of nonspecifically bound streptavidin molecules to bare SiO_2 substrates under static (black square) and lateral (red triangle) flow conditions.

Figure 2-8B shows the dissociation curves of nonspecifically adsorbed FITC-labeled streptavidin molecules on bare SiO_2 substrates under static and lateral flow conditions. For the nonspecific adsorptions of streptavidin molecules on bare SiO_2 substrates, bare SiO_2 substrates were incubated in 1 ug/ml streptavidin solution for 12 hours at 4 ℃. The incubated substrates were gently washed with a PBS solution, and the tests were conducted in a PBS solution under static and lateral flow condition for 60 min. The measured fluorescence intensities were fitted by exponential decline functions [26]. Black and red lines indicate the fitting curves of static and lateral flow condition experiments, respectively. The graph shows that fluorescence intensities decreased significantly under lateral flow conditions, while those barely changed under static conditions. These results clearly showed that the nonspecifically adsorbed streptavidin molecules can be reduced by lateral flows.

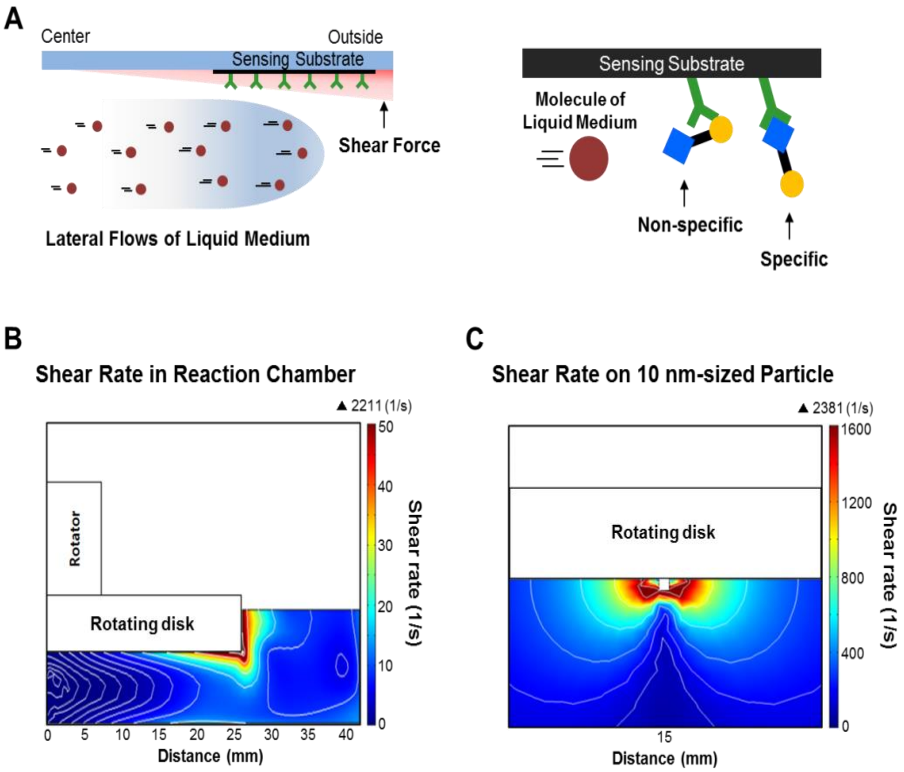

Figure 2-9. Shear forces on a biosensor (A) Schematic diagrams depicting the generation of shear forces (B) Simulation results of a shear rate distribution in a reaction chamber (C) Simulation results of a shear rate distribution on a 10 nm-sized particle attached on 15 mm from the center of the disk. The rotating speed of a rotating disk was set to 150 rpm.

A plausible explanation of the reduced non-specific reactions can be shear forces under a lateral flow condition (Figure 2-9A). Once lateral flows occur around the biosensor, a shear force is generated by collisions between the biosensor surface and the molecules of a liquid medium. At this time, the shear force can act as a force for removing the bound molecules on the sensor surface. By comparing the bonding force of the bound molecules with the magnitude of the shear force, it is possible to predict the bonding or removal of bound molecules. To estimate shear forces generated by lateral flows in our experiments, we first conducted the simulation of shear rate distributions around a rotating disk with a 10 nm-sized particle at 15 mm from its center (Figure 2-9B and C). The shear force near the particle was estimated by multiplying the shear rate with the viscosity of water. The estimated shear force on a 10 nm-sized particle was ~2.7 pN. It corresponds to only ~ 1 % of the reported binding force (220 ~ 460 pN) of a single streptavidin-biotin pair [27-29]. On the other hand, it is ~ 10 % of the common nonspecific binding forces (20 ~ 100 pN) between streptavidin molecules and a glass substrate [29]. We summarized the results in table 2-1.

Table 2-1. Comparison of a calculated shear force with specific and nonspecific binding forces

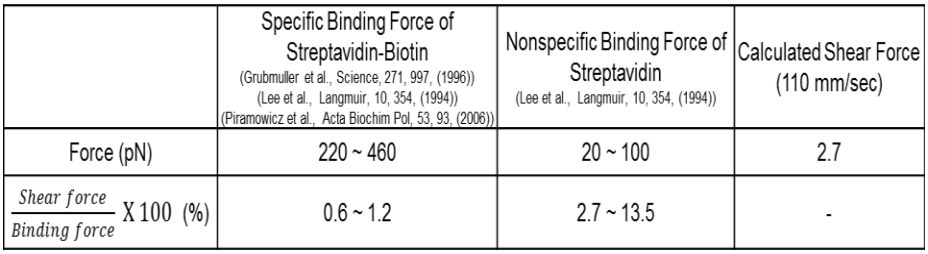

	Specific Binding Force of Streptavidin-Biotin (Grubmuller et al., Science, 271, 997, (1996)) (Lee et al., Langmuir, 10, 354, (1994)) (Piramowicz et al., Acta Biochim Pol, 53, 93, (2006))	Nonspecific Binding Force of Streptavidin (Lee et al., Langmuir, 10, 354, (1994))	Calculated Shear Force (110 mm/sec)
Force (pN)	220 ~ 460	20 ~ 100	2.7
$\frac{Shear\ force}{Binding\ force}$ X 100 (%)	0.6 ~ 1.2	2.7 ~ 13.5	-

The specific binding force of a single streptavidin to biotin molecules would be higher than reported one due to four biotin binding sites in a single streptavidin molecule. Therefore, the shear forces generated by a lateral flow might affect significantly only nonspecific bindings of streptavidin molecules. Since the nonspecific bindings of target molecules could result in back ground noises or false signals in biosensors, our strategy could be used to enhance the selectivity of bio-sensing systems.

2.6 Quantitative Analysis

The change of a binding affinity hinders the quantitative evaluations of biomolecular reactions. The binding affinity of SA-biotin reactions dramatically decreases in low pH [30-32] and low ionic strength [33] conditions. The change of binding affinity in different environmental conditions is due to the change of attraction and repulsion forces between SA and biotin molecules. Attraction and repulsion forces could be explained by a Derjaguin-Landau-Verwey-Overbeek (DLVO) theory [34, 35] which describes the attractive and repulsive forces between charged particles in a liquid medium.

Figure 2-10 shows the schematic diagram depicting a repulsive force change between target and a receptor on a sensor surface in different pH and ionic strength conditions. When two interacting molecules having same electrical charges approach each other, long-range electrostatic repulsive forces between the molecules increase, which obstruct binding interactions between two molecules. Especially, as the pH is lowered, the electrostatic charge of the molecules become more positive, thus, the repulsive force becomes stronger [36]. Finally, the enhanced repulsive force attenuates the performance of the biosensor.

Similar behaviors can be happened in the change of ionic strength conditions. The ionic strength can be calculated as the concentration of ions contained in the liquid medium. The higher ionic concentration indicates the stronger ionic strength. The ions in the medium are attracted on the surface of charged molecules and screen the charges of the molecules [37]. Therefore, the repulsive force between the molecules weakens and they easily approach each other. However, when the ion concentration is lowered, the repulsive force becomes stronger and the reactivity between the molecules decreases because the screening effect that blocks the charges of the molecules is attenuated.

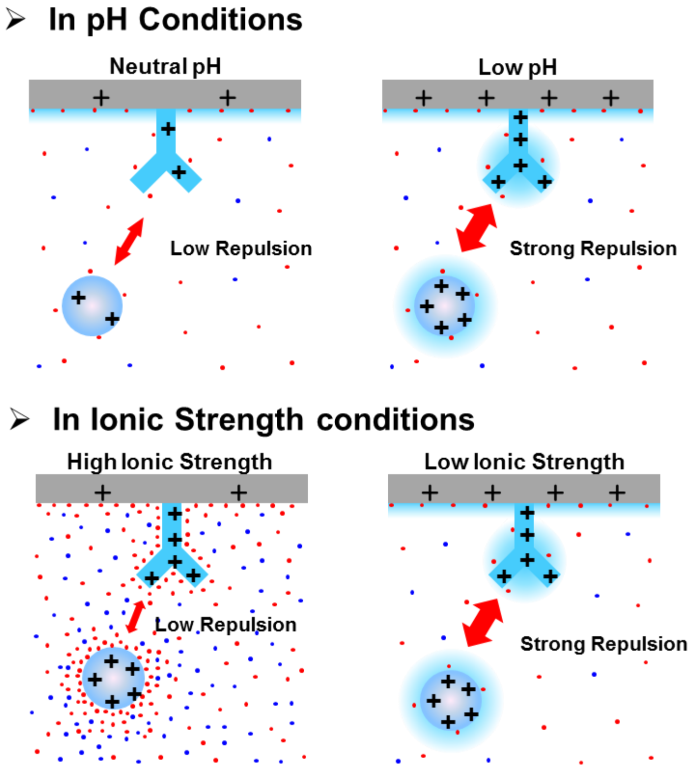

Figure 2-10. Schematic diagram depicting a repulsive force change between target and a receptor on a sensor surface in different pH and ionic strength conditions

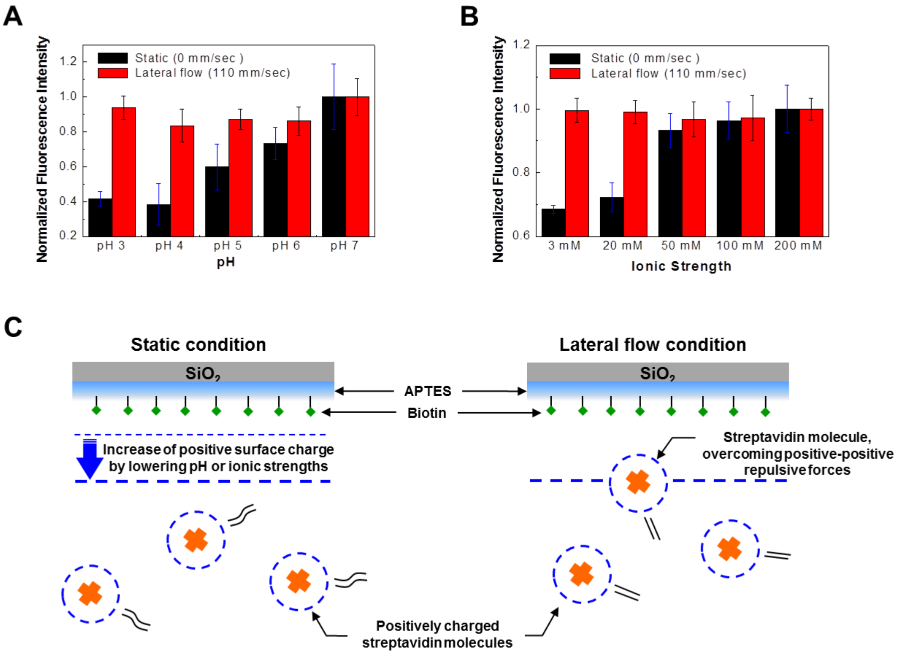

Figure 2-11. Effect of lateral flows on streptavidin-biotin reactions under various pH and ionic strength conditions: (A) Normalized fluorescence intensities of bound FITC-labeled streptavidin molecules on biotinylated substrates under different pH and flow speed conditions; (B) Normalized fluorescence intensities of bound FITC-labeled streptavidin molecules on biotinylated substrates under different ionic strength and flow speed conditions; (C) Schematic diagrams depicting the movements of streptavidin molecules to a biotinylated substrate under i) a static condition and ii) a lateral flow condition in low pH or low ionic strength solution.

Figure 2-11A shows the normalized fluorescence intensities of bound FITC-labeled streptavidin molecules on biotinylated substrates under different pH and flow speed conditions. For preparing streptavidin solutions with various pH values, we dissolved FITC-labeled streptavidin powders in citric acid-Na_2HPO_4 buffer solutions which were titrated to have pH ranges from 3 to 7. The sensing experiments were conducted under static and lateral flow conditions in different pH value target solution for 2 hours. The obtained fluorescence intensities were normalized with respect to the result at pH 7. The fluorescence intensities of bound FITC-labeled streptavidin molecules under static conditions (black bars) are decreased with the decrease of pH values. Previous works showed that at a low pH condition, many of receptor molecules lose their binding affinity and sensor devices based on the receptor do not work [30-32], which is consistent with our results. On the other hand, it should be pointed out that the fluorescence intensities under lateral flow conditions (red bars) are almost similar over the entire pH range, indicating the same amount of bound streptavidin on the biotinylated substrate. These results show that under lateral flow conditions, biotins on the substrate maintained its affinity to streptavidin, and the biotinylated substrate can be used as a sensor device even in the very low pH of the target solution.

We also performed a similar experiment of FITC-labeled streptavidin binding onto biotinylated substrates under different ionic strength and flow speed conditions (Figure 2-11B). For preparing streptavidin solutions with different ionic strength, 1 M NaCl solutions were added to sodium acetate buffer solutions (pH 5) to have the ionic strength range from 3 mM to 200 mM. Then, FITC-labeled streptavidin powders were dissolved in the solutions to have 1 ng/ml of streptavidin concentrations. The fluorescence intensities of bound FITC-labeled streptavidin molecules under static conditions (black bars) are reduced with a decrease in ionic strengths. Presumably, at a low ionic strength, the binding affinity of biotin onto streptavidin became weak as reported previously[33]. Interestingly, fluorescence intensities under lateral flow conditions (red bars) are maintained regardless of ionic strength changes. These results imply that the binding affinity of streptavidin-biotin reactions was maintained by the lateral flows of target solution even in low ionic strength conditions. Such an improved binding affinity under a lateral flow conditions has not been reported before.

Figure 2-11C shows schematic diagrams depicting a plausible explanation of the improved binding affinity observed in our experiments under a lateral flow condition. It shows the movement of streptavidin molecules to a biotinylated biosensor under i) a static and ii) a lateral flow conditions in low pH or low ionic strength solutions. Previous works show that the decrease of binding affinity between interacting molecules in low pH or low ionic strength solutions can be explained by the net electrical charge of molecules [34, 35]. When two interacting molecules having same electrical charges approach each other, long-range electrostatic repulsive forces between the molecules increase, which obstruct binding interactions between two molecules. The net electrical charges of streptavidin molecules and biotinylated SiO_2 substrates were reported to have positive values below a pH of 6 [34, 36, 38]. These positive charges increase as pH or ionic strengths decrease, which enhances repulsive forces between streptavidin molecules and biotinylated surfaces. Therefore, binding reactions between streptavidin and biotin molecules can be attenuated by lowering pH or ionic strengths of a liquid medium (Figure 2-11C i)).

On the other hand, under a lateral flow condition in figure 2-11C ii), the lateral flows increase the molecular speed of streptavidin molecules as well as the mass transfer rates of the molecules to a biotinylated surface. Presumably, the increased molecular speeds and mass transfer rates could help overcoming electrostatic repulsive forces between streptavidin molecules and the biotinylated substrate and enhance the probability of the existence of streptavidin molecules near the biotinylated surface. It could induce the increase in effective collisions between streptavidin and biotin molecules under a lateral flow condition, which allows the binding rate of streptavidin-biotin molecules to be maintained even under low pH and ionic conditions. In many bio-sensing systems, the changes of the environmental conditions of target solutions hinder the quantitative detections of target molecules. Thus, our lateral flow strategy could also be a powerful tool for developing a quantitative bio-sensing system without worries about environmental conditions.

2.7 Summary

In conclusions, we report a high-speed lateral flow strategy for a fast bio-sensing with an improved selectivity and binding affinity even under harsh conditions. In this strategy, to create a high-speed lateral flow (flow speed ~ 110 mm/s) of a target solution with respect to a biosensor, the biosensor was fixed at a location away from the center of a rotating disk, and the disk rotated with a rather high speed (~ 150 rpm) during the sensing measurement. We found that the outermost biosensors, which are 15 mm from the center of the disk, showed the 60 % improved binding rate of target molecules than the innermost biosensors at the center of the disk, which directly showed the importance of the lateral flow speeds on biosensor characteristics. Interestingly, weakly-bound molecules on the biosensor surface were removed by shear forces from laterally-moving solution, which, in effect, removed non-specifically bound molecules and improved the selectivity of biosensors. Furthermore, we found that the binding affinity between target molecules and sensing molecules was enhanced even under very harsh conditions such as acidic pH 3 and the low ionic concentration of 3 mM, which can be important in improving the detection limit of biosensors in real samples. These results show that the performance of conventional biosensors can be improved simply by moving sample solution laterally with a high speed, and, thus, our lateral flow strategy can be a simple but powerful tool for versatile bio- and medical applications.

2.8 References

[4] Driskell J. D.; Uhlenkamp J. M.; Lipert R. J.; Porter M. D., *Analytical Chemistry,* **2007**, 79, 4141-4148.

[13] Wang G. F.; Driskell J. D.; Hill A. A.; Dufek E. J.; Lipert R. J.; Porter M. D., *Annual Review of Analytical Chemistry, 3,* **2010**, 3, 387-407.

[19] Lapin N. A.; Chabal Y. J., *J Phys Chem B,* **2009**, 113, 8776-8783.

[20] Zhang Z. P.; Yoo R.; Wells M.; Beebe T. P.; Biran R.; Tresco P., *Biomaterials,* **2005**, 26, 47-61.

[21] Srisa-Art M.; Dyson E. C.; Demello A. J.; Edel J. B., *Analytical Chemistry,* **2008**, 80, 7063-7067.

[22] Lee M.; Jung J. W.; Kim D.; Ahn Y. J.; Hong S.; Kwon H. W., *Acs Nano,* **2015**, 9, 11728-11736.

[23] Hilton D. J.; Zhang J. G.; Metcalf D.; Alexander W. S.; Nicola N. A.; Willson T. A., *Proceedings of the National Academy of Sciences of the United States of America,* **1996**, 93, 497-501.

[24] Wang G. F.; Driskell J. D.; Porter M. D.; Lipert R. J., *Analytical Chemistry,* **2009**, 81, 6175-6185.

[25] Volkan-Kacso S.; Marcus R. A., *Proceedings of the National Academy of Sciences of the United States of America,* **2015**, 112, 14230-14235.

[26] Wang W. R.; Lu P.; Fang Y. L.; Hamuro L.; Pittman T.; Carr B.; Hochman J.; Prueksaritanont T., *Drug Metabolism and Disposition,*

2011, 39, 1469-1477.

[27] Piramowicz M. D.; Czuba P.; Targosz M.; Burda K.; Szymonski M., *Acta Biochimica Polonica,* **2006**, 53, 93-100.

[28] Grubmuller H.; Heymann B.; Tavan P., *Science,* **1996**, 271, 997-999.

[29] Lee G. U.; Kidwell D. A.; Colton R. J., *Langmuir,* **1994**, 10, 354-357.

[30] Kohler M.; Karner A.; Leitner M.; Hytonen V. P.; Kulomaa M.; Hinterdorfer P.; Ebner A., *Molecules,* **2014**, 19, 12531-12546.

[31] Hofmann K.; Wood S. W.; Brinton C. C.; Montibeller J. A.; Finn F. M., *Proc Natl Acad Sci U S A,* **1980**, 77, 4666-4668.

[32] Green N. M., *Biochem J,* **1966**, 101, 774-780.

[33] Holmberg A.; Blomstergren A.; Nord O.; Lukacs M.; Lundeberg J.; Uhlen M., *Electrophoresis,* **2005**, 26, 501-510.

[34] Leckband D. E.; Schmitt F. J.; Israelachvili J. N.; Knoll W., *Biochemistry,* **1994**, 33, 4611-4624.

[35] Yeung C.; Leckband D., *Langmuir,* **1997**, 13, 6746-6754.

[36] Wise N.; Grob T.; Morten K.; Thompson I.; Sheard S., *Journal of Magnetism and Magnetic Materials,* **2015**, 384, 328-334.

[37] Majhi P. R.; Ganta R. R.; Vanam R. P.; Seyrek E.; Giger K.; Dubin P. L., *Langmuir,* **2006**, 22, 9150-9159.

[38] Yamada K.; Yoshii S.; Kumagai S.; Fujiwara I.; Nishio K.; Okuda M.; Matsukawa N.; Yamashita I., *Japanese Journal of Applied Physics Part 1-Regular Papers Brief Communications & Review Papers,* **2006**, 45, 4259-4264.

Chapter 3

Electrical Noise Analysis in PEDOT:PSS Conducting Polymer Film for High Performance Bio-sensing Devices

3.1 Electrical Noise in Bio-sensing Device

Electrical biosensors based on conducting polymers have been widely developed due to their flexibility, fast response speed and no need for a labeling technique. However, electric-based biosensors have a fundamental limitation in detection sensitivity resulted from electrical noise signals. For example, recently, PEDOT:PSS conducting polymers has been utilized as a biosensor material because of its high conductivity, flexibility, and bio compatibility [39-41]. However, relatively high electrical noises have made it difficult to accurately analyze the bio-activity signals. By solving the electric noise problem in an electric-based biosensor, we could expect the development of an improved biosensor.

3.2 Scanning Noise Microscopy

Fig. 3-2 shows the schematic diagram of our SNM system for imaging current and noise signals on a PEDOT:PSS film. For current and noise measurements, a platinum (Pt) probe installed on a conductive AFM (XE-70, Park Systems Corp.) was directly contacted with the surface of a spin-coated PEDOT:PSS film with 100 nN of a contact force. A desired DC bias voltage between the probe and Au substrate was applied using a DC power supplier (DS345, Stanford Research Systems), and current signals were acquired through the probe. The acquired current signals were amplified by a low-noise preamplifier (SR570, Stanford Research Systems). In the spectrum analyzer, the measured current signals were filtered by the band-pass filter at a specific frequency range to obtain the electrical noise signals, and the RMS power of the noise signals were acquired by a RMS-to-DC converter [42-44]. Note that, since the measured RMS power is the integrated value of the noise powers over the frequency range of the used band-pass filter, the noise powers were divided by the bandwidth of the band-pass filter to get an absolute noise power spectral density (PSD) at the central frequency of the pass band. Finally, we could simultaneously obtain the maps of currents and noise PSDs at a specific frequency by scanning the probe over the surface of the PEDOT:PSS film. For minimizing possible oxidation and humidity effects on PEDOT:PSS films during the measurements, all measurements were conducted in N_2 atmosphere.

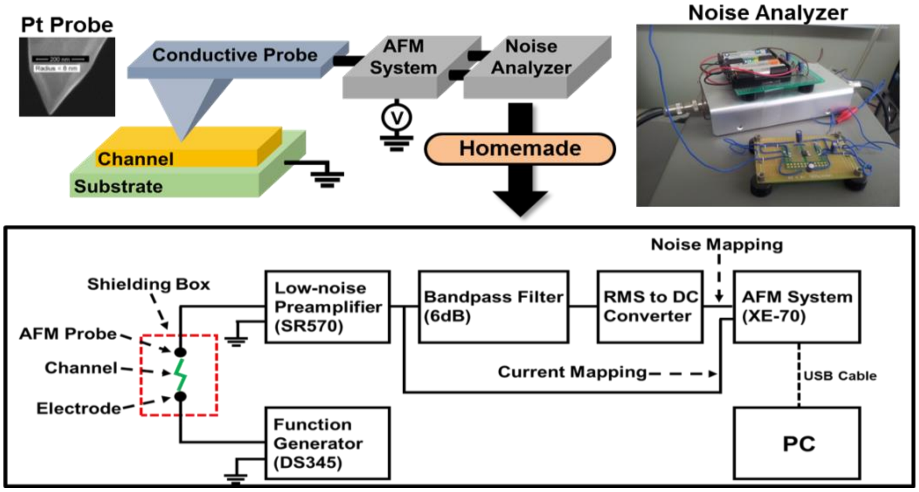

Figure 3-2. Schematic diagram of a scanning noise microscopy (SNM) system

3.3 Basic Characteristics of a PEDOT:PSS Film

The chemical structures of PEDOT and PSS polymers were shown in figure 3-3. PEDOT is a conjugated polymer with alternating single and double bonds along its backbone. PSS monomers have a phenyl ring with one acidic SO_3H group. When PSS polymers are mixed with PEDOT, some of PSS monomers form negatively-charged SO_3^- groups which enable PEDOT polymers to be dispersed well in an aqueous solution.

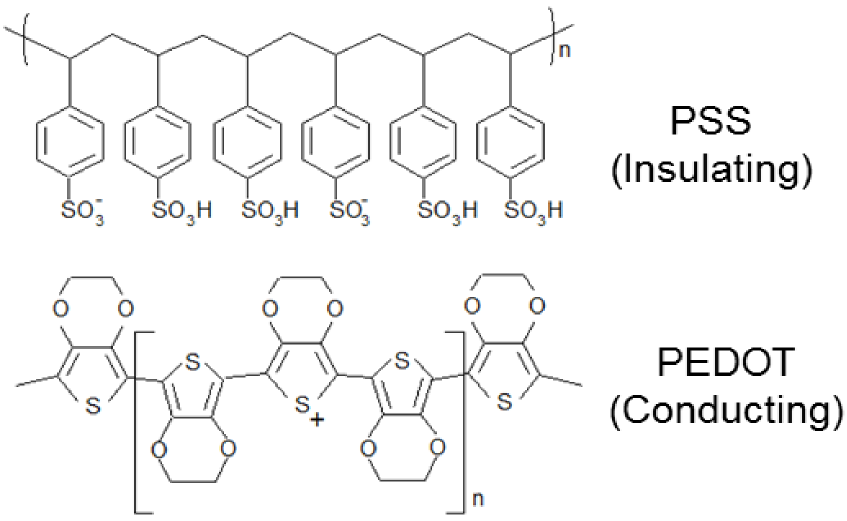

Figure 3-3. Chemical structures of PEDOT and PSS polymer chains

Figure 3-4A shows the schematic diagram of a PEDOT:PSS film spin-coated on an Au substrate. Since PEDOT:PSS polymers are the mixture of two different polymers, PEDOT-rich and PSS-rich regions exist in the film [45, 46]. We prepared PEDOT:PSS film samples by using a spin coating method on Au film substrates. Briefly, 1.3 wt% PEDOT:PSS dispersions (Dispersed in H_2O, weight ratio = 1:1.6) were purchased from Sigma-Aldrich for SNM measurements. The PEDOT:PSS dispersion was spin-coated on an Au substrate (10 nm Ti / 40 nm Au on a SiO_2) with 3000 rpm for 60 seconds to form the thin film layer of PEDOT:PSS polymers. Then, the coated PEDOT:PSS samples were annealed at 140 ℃ in N_2 atmosphere conditions for 1 hr.

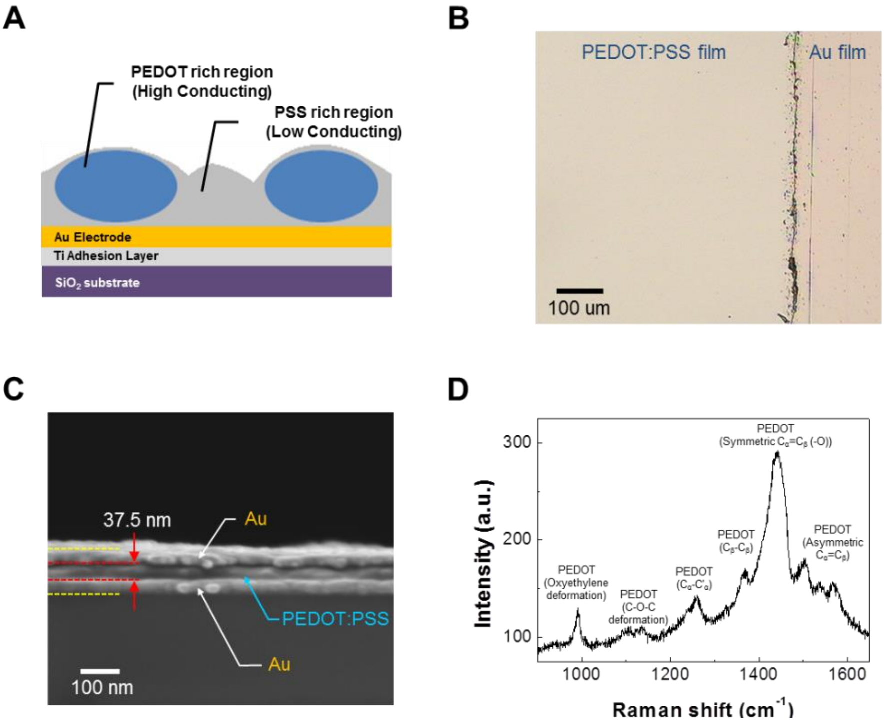

Figure 3-4. Basic characteristics of a PEDOT:PSS film (A) Schematic diagram of a PEDOT:PSS film spin-coated on an Au substrate (B) Optical microscope image of a PEDOT:PSS film. (C) SEM image of a PEDOT:PSS film with a cross sectional view. (D) Raman spectra of a PEDOT:PSS film.

Figure 3-4B shows the optical microscope image of a PEDOT:PSS film on an Au film substrate. The sample was prepared by a spin-coating method as described in Experimental section, and the Au film substrate was exposed by gently scrubbing out the 1/3 area of the PEDOT:PSS film with a wet cotton swab. The exposed Au film was used as a bottom electrode contact area of the sample. We took an optical image at the boundary of the PEDOT:PSS film. The image shows the PEDOT:PSS film and the Au electrode, and the PEDOT:PSS film shows very clean surface without dusts or wrinkles.

Figure 3-4C shows the scanning electron microscopy (SEM) image of a PEDOT:PSS film with a cross sectional view. For taking the SEM image of the PEDOT:PSS film sample with a cross sectional view, we first deposited another Au film on the top of the sample by using a thermal evaporation method, and then the sample was cleaved by a diamond scriber. The Au films at the top and bottom of the PEDOT:PSS film allowed us to clearly estimate the thickness of the PEDOT:PSS film in the SEM image. The thickness of the PEDOT:PSS film was found ~37.5 nm. Note that it does not show pores in the film, supporting the uniformity of the PEDOT:PSS film.

Figure 3-4D shows the Raman spectra of a PEDOT:PSS thin film. The spectra were obtained using a Raman spectrometer (T64000, HORIBA Jobin Yvon) with a 514 nm excitation laser line. The spectra peak positions of the PEDOT:PSS film were well matched with the asymmetric $C_\alpha=C_\beta$ stretching peaks of PEDOT polymers at 1565 cm^{-1}, 1535 cm^{-1} and 1504 cm^{-1}, the symmetric $C_\alpha=C_\beta$ (-O) stretching peak of PEDOT polymers at 1443 cm^{-1}, the C_β-C_β stretching peak of PEDOT polymers at 1369 cm-1, the C_α-C_α inter-ring stretching peak of PEDOT polymers at 1260 cm^{-1}, the C-O-C deformation peak of PEDOT polymers 1100 cm^{-1}, and the oxyethylene ring deformation peak of PEDOT polymers at 991 cm^{-1} as reported previously [47, 48]. Due to the low intensities of PSS spectra compared to the spectra of PEDOT [47], the spectral peaks of PSS were not observed in the spectra. The results indicate the high purity of the PEDOT:PSS film without contamination.

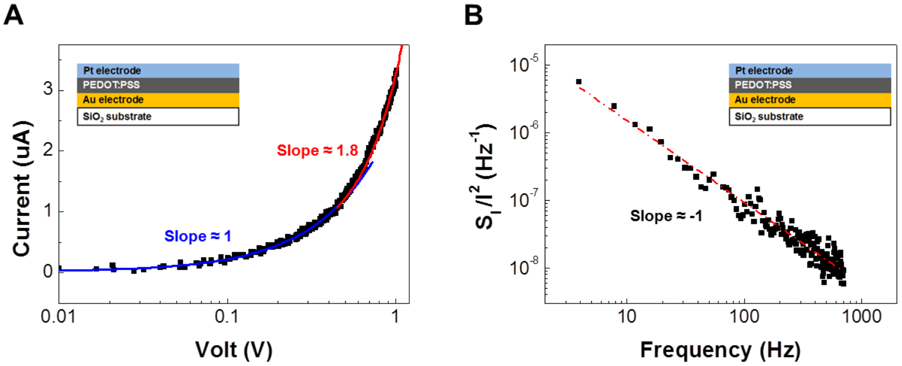

Figure 3-5. Electrical characteristics of a conventional PEDOT:PSS film device (A) Semi-log *I-V* curve of a PEDOT:PSS film (B) Frequency spectra of the current-normalized noise PSD (S_I/I^2) of the PEDOT:PSS film

Figure 3-5A shows the semi-log *I-V* curve of a PEDOT:PSS sample. For measuring the basic electrical characteristics of a PEDOT:PSS film, a Pt film was thermally deposited on the PEDOT:PSS film sample and used as a top electrode. The *I-V* curve showed the gradual increase of currents by increasing voltages. We fitted the curve by the relationship of $I \propto V^{\alpha}$. The slope α in the graph was ~1 at a voltage range from 0 to 0.4 V and ~1.8 from 0.4 to 1 V. Previously, the conduction mechanism of a PEDOT:PSS film were reported to follow a space-charge-limited conduction (SCLC) model [45, 49, 50]. In this model, the slope α of the *I-V* curves were ~1 at low bias voltage regions indicating ohmic behaviors and ~2 at intermediate bias voltage region indicating charge-trap-filled behaviors, which match well with our results.

Figure 3-5B shows the frequency spectra of the current-normalized noise PSD (S_I/I^2) of the PEDOT:PSS sample. The S_I/I^2 was acquired at the applied voltage of 0.06 V in a frequency range from 1 to 700 Hz. The graph shows the frequency dependence of the PSD with $S_I/I^2 \propto f^{\gamma}$, where the exponent of γ was close to ~1 indicating *1/f* noise behaviors of the PEDOT:PSS film as reported previously [51, 52]. Since the *1/f* noise behaviors arise from the superposition of individual noise signals from different charge trapping centers [53], the *1/f* behaviors of the PEDOT:PSS films indicated the existence of many different charge traps in the PEDOT:PSS film.

3.4 SNM Measurement on a PEDOT:PSS Film

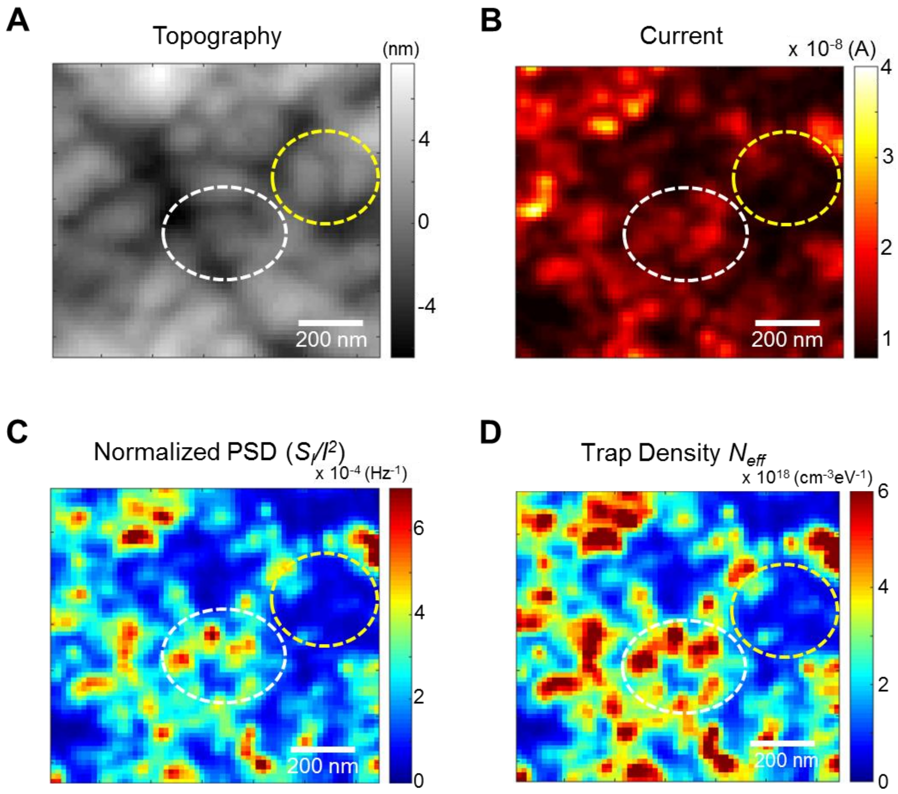

Figure 3-6. Experimental results measured with a SNM system (A) AFM topography image of a PEDOT:PSS film. (B) Current map of the PEDOT:PSS film. The map was measured simultaneously with the topography image. *Yellow-* and *white-dotted circles* show *high-current* and *low-current regions*, respectively. The same marks were also used in figure 3-6 for showing the same regions in each figure. (C) Current-normalized noise PSD (S_I/I^2) map at 50 Hz (D) Effective charge trap density (N_{eff}) map calculated from the S_I/I^2 map

Figure 3-6A shows the AFM topography image of a PEDOT:PSS film on an Au/SiO_2 substrate. During the AFM scanning, the contact force and scan rate of an Pt probe was maintained with 100 nN and 0.1 Hz, respectively. The topography image shows that the PEDOT:PSS film consisted of round-shaped grains with a diameter ranging from 50 to 100 nm. The diameters of grains are relatively larger than the film thickness of 37.5 nm, which implies the flattened balls or pancake-like structures of the PEDOT:PSS grains as reported previously [54].

The current map of the PEDOT:PSS film was measured simultaneously with the topography image (Figure 3-6B). The bias voltage between the Pt probe and the Au electrode was maintained with 0.06 V during the measurement. The current map shows a non-uniform current distribution. The current levels at a high-current region (yellow-dotted circle) and a low-current region (white-dotted circle) are 2 × 10-8 A and 9 × 10-9 A, respectively. Previously, it was reported that the non-uniform current distribution in a PEDOT:PSS film can be attributed to the non-uniform distribution of PEDOT polymers in the film [45, 46, 54]. Since PEDOT polymers have a higher conductivity than PSS [55], we could consider the high-current region and the low-current region as a PEDOT-rich grain and a PSS-rich grain, respectively.

The current-normalized noise PSD (S_I/I^2) value can be a useful parameter to represent electrical-noise characteristics in electronic materials [42, 44]. Fig. 3-6C shows the map of S_I/I^2 (at 50 Hz) estimated from the noise PSD (S_I) map of the PEDOT:PSS film. To obtain the S_I/I^2 map, the S_I map of the PEDOT:PSS film was measured simultaneously with the current map at the bias voltage of 0.06 V, and the S_I map was divided by the square of currents. The S_I/I^2 map shows the significant difference of S_I/I^2 levels between grains. When the S_I/I^2 map is compared with the current map, the high- and the low-current grain show high S_I/I^2 and low S_I/I^2 values, respectively. Since S_I/I^2 values show noise intensities per unit current, these results imply more noise sources in the high-current grain than the low-current grain at that bias voltage.

Previously, we reported a method to quantitatively estimate the density of localized charge traps in electrical materials using a SNM system [42, 44, 56]. Here, we assumed that the measured $1/f$ noises in a PEDOT:PSS film were generated by carrier-number fluctuations as suggested previously [51, 52, 57]. Since the charge carriers are captured and released by charge traps with a random process, the number of occupied traps fluctuate currents randomly with time, generating electrical noises. Considering a conducting AFM probe in contact with a PEDOT:PSS surface at the position (x, y), the PSD at the position can be written like [58-60],

$$S_{N_t}(f,x,y) = \Delta x \Delta y \cdot \int_{-\infty}^{\infty} \int \frac{4\tau(E,x,y,z)}{1+[2\pi f \cdot \tau(E,x,y,z)]^2} \cdot f_t(1-f_t) \cdot N_t(E,x,y,z) \cdot dz \cdot dE \quad (1)$$

where the N_t, f_t, f, and τ are the density of traps over space and energy, a trap occupancy function, a frequency, and a trapping time constant, respectively. An integration in the z direction (vertical direction to the film surface) ranges from 0 to the thickness of a PEDOT:PSS film. At room temperature, f_t $(1\text{-}f_t)$ behaves like a delta function around the Fermi level, and the equation (1) after the integration over electron energy E can be written as [61]

$$S_{N_t}(f,x,y) = \Delta x \Delta y \cdot kT \cdot \int \frac{4\tau(E_f,x,y,z)}{1+[2\pi f \cdot \tau(E_f,x,y,z)]^2} \cdot N_t\left(E_f,x,y,z\right) \cdot dz \quad (2)$$

Here, we define the effective trap density N_{eff} like

$$N_{eff}(f,x,y) \equiv f \cdot \int \frac{4\tau(E_f,x,y,z)}{1+[2\pi f \cdot \tau(E_f,x,y,z)]^2} \cdot N_t\left(E_f,x,y,z\right) \cdot dz \quad (3)$$

Then, the equation (2) can be simply rewritten as

$$S_{N_t}(f,x,y) = \frac{kT}{f} N_{eff}(f,x,y) \cdot \Delta x \Delta y \quad (4)$$

We can write the PSD of the current noises S_I generated by the segment as [58]

$$S_I(f,x,y) = \frac{(I)^2}{(\Delta C)^2} S_{N_t}(f,x,y) = \frac{(I)^2}{(\Delta C)^2}\frac{kT}{f} N_{eff}(f,x,y)\,\Delta x\Delta y \tag{5}$$

with the number of charge carriers ΔC in the area $\Delta x\Delta y$ and current I through the small segment of the PEDOT:PSS film. Then, N_{eff} can be written as

$$N_{eff}(f,x,y) = \frac{(\Delta C)^2}{(I)^2}\frac{f}{kT}\cdot\frac{S_I(f,x,y)}{\Delta x\Delta y} \tag{6}$$

Figure 3-6D shows the effective charge trap density (Neff) map of the PEDOT:PSS film calculated from equation (6). The map showed high N_{eff} at the high-current grain and low N_{eff} at the low-current grain. The trap densities in the high- and low-current grains were about 7×10^{18} cm^{-3}eV^{-1} and 7×10^{16} cm^{-3}eV^{-1}, respectively. The average N_{eff} of the measured region was about 1.08 x 10^{18} cm^{-3}eV^{-1}, which is a similar to the previously-reported value [50]. Previously, it was reported that the insulating grain boundaries in organic conducting materials hinder the flows of charge carriers from one conductive grain to others, therefore, the carriers are trapped inside the grain [54, 62-64]. In addition, charge transport in a PEDOT:PSS film is caused by the hopping process between PEDOT filaments consisting of a PEDOT-rich core with a PSS-rich shell [65]. Therefore, we could assume that electrical noises are generated by charge trapping and releasing from one PEDOT filament to other filament, and PEDOT filaments could be considered as charge trap sites in a PEDOT:PSS film. Note that, since PEDOT filaments are more present in a PEDOT-rich grain than in a PSS-rich grain, higher charge trap densities are expected in the PEDOT-rich grain, which are consistent with our results.

3.5 Voltage Dependence of Effective Charge Trap Density N_{eff}

Figure 3-7 shows the effective charge trap density (Neff) maps of the film under various bias voltage conditions. We repeated noise microscopy measurements on the same position of the PEDOT:PSS film to obtain current and SI maps under various bias voltage conditions. In the figure, we marked high-current (PEDOT-rich grain) and low-current grains (PSS-rich grain) with red- and blue-dotted boxes, respectively. For the direct comparison of Neff maps, same scale bar ranging from 0 to 6 × 1018 cm-3 eV-1 was used.

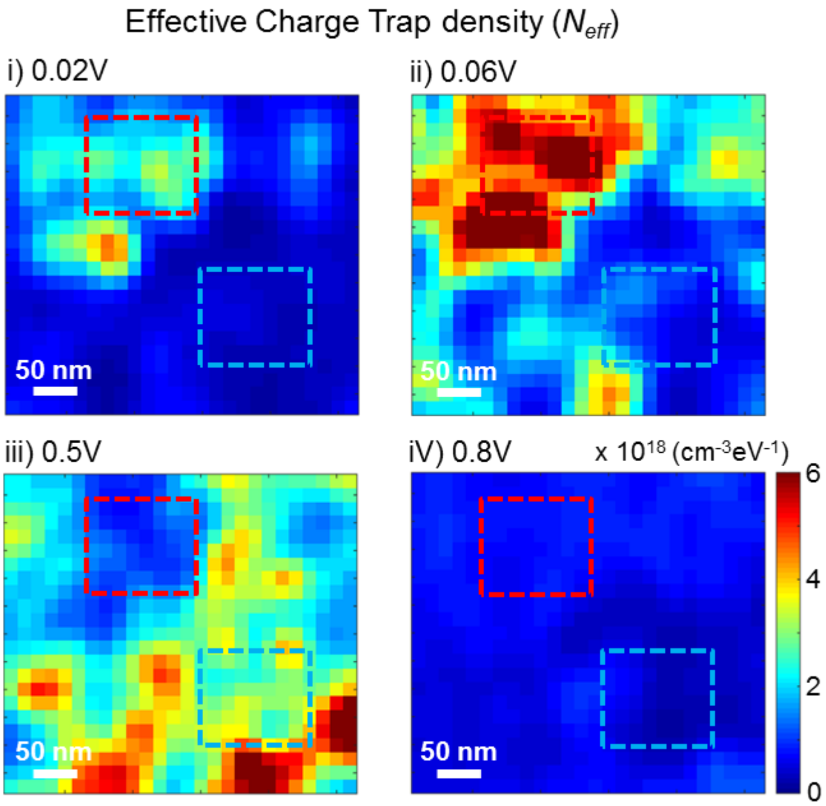

Figure 3-7. Voltage dependence of effective trap density N_{eff} in a PEDOT:PSS film. *Red-* and *blue-dotted boxes* indicate *high* and *low-current grain region*s, respectively.

At low bias voltages of 0.02V and 0.06V (Figure 3-7-i and ii), the high-current grains (red-dotted box) showed higher N_{eff} than low-current grains (blue-dotted box). However, interestingly, the N_{eff} levels in the both regions were suddenly inverted at 0.5 V (Figure 3-7-iii), i.e., the high-current grains showed lower N_{eff} levels than the low-current grains. Moreover, at 0.8V (Figure 3-7-iv), all the measured area suddenly showed very low N_{eff} levels. It should be mentioned that most of the previous results show an increased noise source density at a high bias voltage condition [42, 66]. Moreover, the regions with a high conductivity were usually reported to exhibit a low noise source density [44, 56], presumably, because noise sources such as charge traps usually degrade its carrier mobility and conductivity. To the best of our knowledge, these anomalous behaviors such as the charge trap density inversion or the sudden decrease of charge trap densities by an increased bias voltage were not observed in any other systems before.

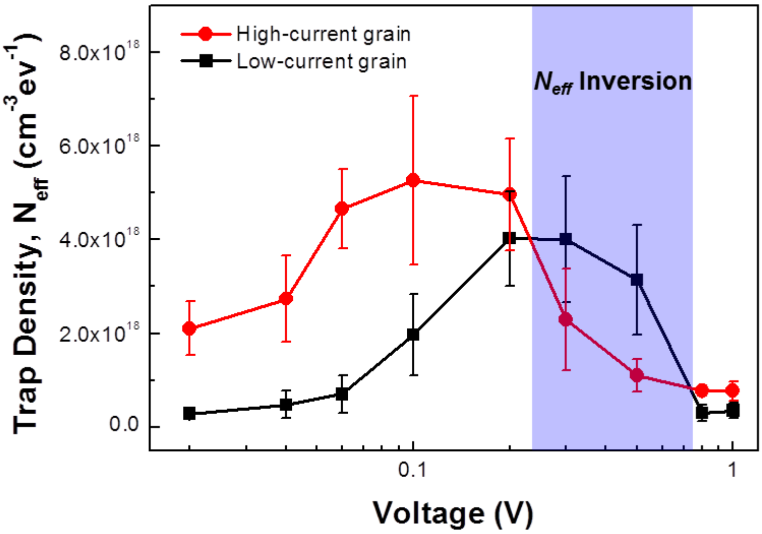

Figure 3-8. N_{eff}-V curves at the high- and low-current grains

To understand these anomalous inversion behaviors, we measured N_{eff} levels at high- and low-current grains under different bias voltages (Figure 3-8). Here, we first obtained N_{eff} maps under various bias voltages by the SNM system, and the averaged N_{eff} values of high- and low-current grains were acquired from the N_{eff} maps. The N_{eff}-V graph at the high-current grain shows changes in N_{eff} levels with an increasing bias voltage. Specifically, as the bias voltage increased, the N_{eff} levels of the high-current grain increased and reached its maximum level at the bias voltage of 0.1 V. Then, the N_{eff} levels decreased and reached the almost minimum level at the bias voltage of 0.5 V. The similar tendency of the lower N_{eff}-V curve was also found in the low-current grain, but the maximum and minimum N_{eff} levels were observed at different voltages of 0.3 V and 0.8 V, respectively. Overall, the N_{eff}-V curves of both high- and low-current grains show anomalous N_{eff} switching as a bias voltage increases. Note that at the bias voltage range of 0 ~ 0.22 V, the high current regions exhibited a higher charge trap density than the low current regions. However, in the bias between 0.22 V and 0.72 V, the high current regions exhibited a lower charge trap density than the high current regions, which is consistent with the contrast inversion of charge trap density shown in figure 3-7. These results indicate that the anomalous inversion in the charge trap density map was because each region had different transition voltages at which the charge traps began to decrease.

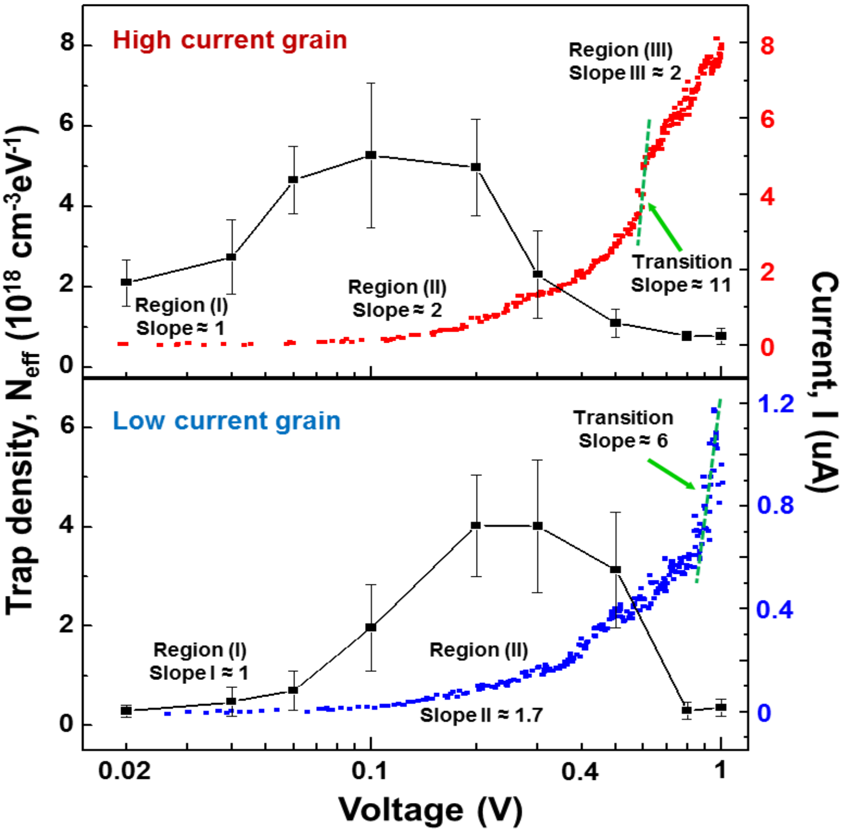

Figure 3-9. N_{eff} -V and I-V curves at the high- and the low-current grains. The current transitions were marked with green arrows.

To investigate the effect of charge trap densities on the electrical characteristics of a PEDOT:PSS film, we plotted charge trap density (N_{eff}) and current level versus bias voltages (Figure 3-9). The I-V curves of both grains show the increase of current levels as the bias voltage increases. Importantly, the abrupt current transitions (green arrows) in the high- and low-current grains were observed at the bias voltages of 0.6 V and 0.9 V, respectively. Previously, the SCLC model was proposed to explain the *I-V* curves in PEDOT:PSS samples, where the abrupt current transition was attributed to the transition of a conduction mechanisms depending on the applied bias voltages [50, 67, 68]. In this case, *I-V* curves can be divided into the distinctive regions with different conduction behaviors, and individual regions can be fitted by $I \propto V^{\alpha}$ with a different scaling parameter α like ohmic region (α ~ 1), charge-trapped behavior region (α ~ 2), current transition region ($\alpha > 2$) and charge-trap-free behavior region (α ~ 2). Note that the *I-V* curve (upper) from the high-current regions can be fitted by $I \propto V^{\alpha}$ with the scaling parameter α of ~ 1, ~ 1.8, ~ 11, and ~ 2, corresponding to the ohmic, charge-trapped behavior, current transition, and charge-trap-free behavior regions in the SCLC model, respectively. We could also observe similar regions with different α of ~ 1, ~ 1.7, and ~ 6 at the low-current grain. However, the current transition in a high current grain (upper) began lower bias voltages than in the low-current grain (lower). Importantly, in both high-current (upper) and low-current regions (lower), the charge trap densities began to decrease and reach a minimal value near the bias voltages for the current transition.

These results indicate that charge traps, which generate electrical noises, strongly affect the electrical characteristics of a PEDOT:PSS film as proposed in the SCLC model [68, 69]. Presumably, at a medium bias voltage range with charge-trapped behavior ($\alpha \sim 2$), some weekly-bound charge carriers captured by charge traps were released by external bias voltages [68]. In this case, the released charge traps could work as additional noise sources and additional hopping conduction paths, resulting in increased noise source density N_{eff} and conductivity, respectively. However, as the bias voltage increased further toward the rather high bias voltage of current transition region ($\alpha > 2$), the charge trap sites were gradually occupied by injected charge carriers [68, 70, 71]. Once the trap sites were occupied with the charge carriers, the occupied trap sites did not work as a noise sources, resulting in the decreased noise source density N_{eff}. After all the trap sites were filled up, active charge traps did not exist, and the subsequently injected carriers should be free to move in the material, resulting in a minimal noise source density and rapid increase of currents as we observed (Figure 3-9). We summarized the distinctive voltage ranges at the high- and low-current grain of PEDOT:PSS film in table 3-1.

Table 3-1. Distinctive voltage ranges at the high- and low-current grains

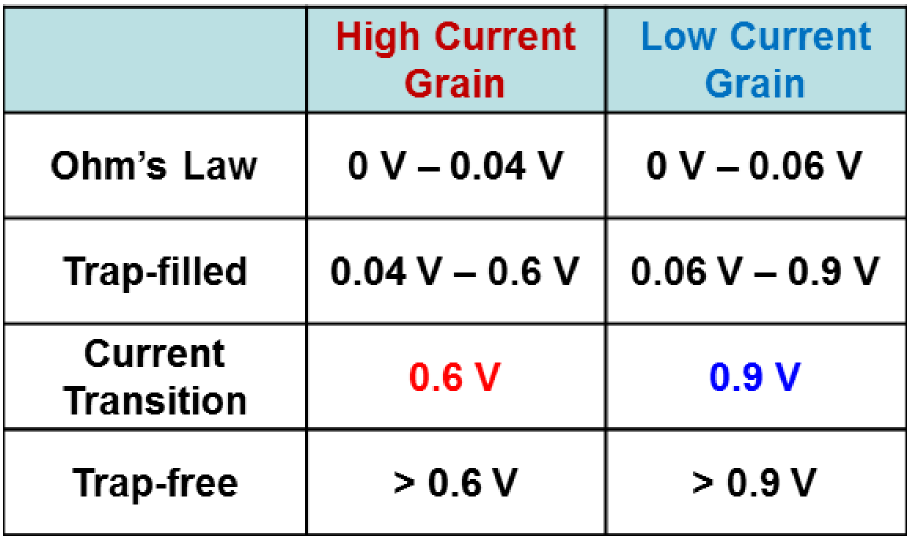

	High Current Grain	Low Current Grain
Ohm’s Law	0 V – 0.04 V	0 V – 0.06 V
Trap-filled	0.04 V – 0.6 V	0.06 V – 0.9 V
Current Transition	0.6 V	0.9 V
Trap-free	> 0.6 V	> 0.9 V

It should be mentioned that, though such a filling phenomenon of charge traps was proposed to explain the abrupt current transition behaviors in the SCLC model, the reduction of charge trap activities was not directly observed. These results clearly imply that our method can be utilized to map the nanoscale effect of charge traps on the charge transport phenomena in conducting films.

3.6 Summary

In conclusion, we observed anomalous noise source switching behaviors and their effects on the trap-free transitions of currents in a

PEDOT:PSS film by using a scanning noise microscopy (SNM) system. The SNM system enabled us to measure the electrical current and noise maps on a PEDOT:PSS film under various bias voltage conditions. The measured maps of the currents and noises were utilized to calculate effective charge trap densities in the film. As results, we found the non-homogeneous distribution of current levels and effective charge trap densities in the film due to the non-uniform distribution of PEDOT-rich and PSS-rich grains. PEDOT-rich grains showed high current level and high charge trap densities, on the other hand, PSS-rich grains showed low current level and low charge trap densities at a low bias voltage. Interestingly, the charge trap densities in both grains showed a switching behavior by applied bias voltages, and the behavior strongly affected to the electrical characteristic of the grains. These results indicated that the charge traps in a PEDOT:PSS film play an important role in the electrical characteristics of the films. Our observations provide a valuable insight on the understanding of the electrical behavior of PEDOT:PSS films and an important guideline to its practical applications.

3.7 References

[39] Khodagholy D.; Doublet T.; Quilichini P.; Gurfinkel M.; Leleux P.; Ghestem A.; Ismailova E.; Herve T.; Sanaur S.; Bernard C.; Malliaras G. G., *Nature Communications,* **2013**, 4.

[40] Wisitsoraat A.; Pakapongpan S.; Sriprachuabwong C.; Phokharatkul D.; Sritongkham P.; Lomas T.; Tuantranont A., *Journal of Electroanalytical Chemistry,* **2013**, 704, 208-213.

[41] Moczko E.; Istamboulie G.; Calas-Blanchard C.; Rouillon R.; Noguer T., *Journal of Polymer Science Part a-Polymer Chemistry,* **2012**, 50, 2286-2292.

[42] Shekhar S.; Cho D.; Lee H.; Cho D. G.; Hong S., *Nanoscale,* **2016**, 8, 835-842.

[43] Engelson M.; Engelson M., *Modern spectrum analyzer theory and applications*. Dedham, Mass.: Artech House, 1984.

[44] Lee H.; Cho D.; Shekhar S.; Kim J.; Park J.; Hong B. H.; Hong S., *Acs Nano,* **2016**, 10, 10135-10142.

[45] Kemerink M.; Timpanaro S.; de Kok M. M.; Meulenkamp E. A.; Touwslager F. J., *Journal of Physical Chemistry B,* **2004**, 108, 18820-18825.

[46] Timpanaro S.; Kemerink M.; Touwslager F. J.; De Kok M. M.; Schrader S., *Chemical Physics Letters,* **2004**, 394, 339-343.

[47] Farah A. A.; Rutledge S. A.; Schaarschmidt A.; Lai R.; Freedman J. P.;

Helmy A. S., *Journal of Applied Physics,* **2012**, 112.

[48] Garreau S.; Duvail J. L.; Louarn G., *Synthetic Metals,* **2001**, 125, 325-329.

[49] Jeong H. Y.; Kim J. Y.; Yoon T. H.; Choi S. Y., *Current Applied Physics,* **2010**, 10, E46-E49.

[50] Rutledge S. A.; Helmy A. S., *Journal of Applied Physics,* **2013**, 114.

[51] Son H. J.; Kwon I. W.; Lee H. C., *Applied Physics Express,* **2009**, 2.

[52] Son H. J.; Kwon I. W.; Lee Y. S.; Lee H. C., *Ieice Transactions on Electronics,* **2009**, E92c, 702-707.

[53] Balandin A. A., *Nature Nanotechnology,* **2013**, 8, 549-555.

[54] Nardes A. M.; Kemerink M.; Janssen R. A. J.; Bastiaansen J. A. M.; Kiggen N. M. M.; Langeveld B. M. W.; van Breemen A. J. J. M.; de Kok M. M., *Advanced Materials,* **2007**, 19, 1196-1200.

[55] Lee T. W.; Chung Y. S., *Advanced Functional Materials,* **2008**, 18, 2246-2252.

[56] Cho D.; Lee H.; Shekhar S.; Yang M.; Park J. Y.; Hong S., *Scientific Reports,* **2017**, 7.

[57] Stoop R. L.; Thodkar K.; Sessolo M.; Bolink H. J.; Schonenberger C.; Calame M., *Physical Review Applied,* **2017**, 7.

[58] Kogan S., *Electronic noise and fluctuations in solids*. Cambridge England ; New York, NY, USA: Cambridge University Press, 1996.

[59] Jayaraman R.; Sodini C. G., *Ieee Transactions on Electron Devices,* **1989**, 36, 1773-1782.

[60] Celikbutler Z.; Hsiang T. Y., *Ieee Transactions on Electron Devices,* **1988**, 35, 1651-1655.

[61] Hooge F. N.; Kleinpenning T. G. M.; Vandamme L. K. J., *Reports on Progress in Physics,* **1981**, 44, 479-532.

[62] Kaake L. G.; Barbara P. F.; Zhu X. Y., *Journal of Physical Chemistry Letters,* **2010**, 1, 628-635.

[63] Hallam T.; Duffy C. M.; Minakata T.; Aando M.; Sirringhaus H., *Nanotechnology,* **2009**, 20.

[64] Muller E. M.; Marohn J. A., *Advanced Materials,* **2005**, 17, 1410-1414.

[65] van de Ruit K.; Cohen R. I.; Bollen D.; van Mol T.; Yerushalmi-Rozen R.; Janssen R. A. J.; Kemerink M., *Advanced Functional Materials,* **2013**, 23, 5778-5786.

[66] Shekhar S.; Cho D.; Cho D. G.; Yang M.; Hong S., *Nanotechnology,* **2018**, 29.

[67] Syed A. Moiz I. A. K., Waheed A. Younis and Khasan S. Karimov, *IntechOpen,* **2016**.

[68] Chiu F. C., *Advances in Materials Science and Engineering,* **2014**.

[69] Kollath V. O.; Arjmand M.; Egberts P.; Sundararaj U.; Karan K., *Rsc Advances,* **2017**, 7, 32564-32573.

[70] Joung D.; Chunder A.; Zhai L.; Khondaker S. I., *Applied Physics Letters,* **2010**, 97.

[71] Rose A., *Physical Review,* **1955**, 97, 1538-1544.

Chapter 4

Conclusions

In this dissertation, first, we discussed the methods to overcome the fundamental limitations of conventional bio-sensing systems.

First, we developed a high-speed lateral flow strategy for a fast biosensing with an improved selectivity and binding affinity even under harsh conditions. In this strategy, the biosensor was fixed at a location away from the center of a rotating disk, and the disk was rotated at a rather high speed to create the high-speed lateral flow of the target solution on the biosensor surface. Experimental results show that the lateral flow strategy improved various biosensor performances such as the response speed and sensitivity, the reduction of non-specific bindings. Furthermore, the binding affinity between target and receptors was enhanced even under very harsh environmental conditions such as an acidic pH and a low ionic concentration. These results clearly show that the performance of conventional biosensors could be improved simply by moving the sample solution laterally with a high speed.

Next, the electrical noises which determine the detection limit of the bio-sensing system were studied by using a scanning noise microscopy (SNM) system. In this study, we performed the electrical noise analysis in a PEDOT: PSS thin film which is widely used as a biosensor material. The SNM system allowed us to observe current and electrical noise signal distributions with a nanometer resolution in the PEDOT:PSS film. The experimental results show that the noise sources which were charge trap sites were distributed non-uniformly in the PEDOT:PSS film. Moreover, the density of the noise sources showed the anomalous switching behaviors according to the external applied voltage, which were strongly related with the electrical characteristics of the PEDOT:PSS film. This study shows that there are experimental conditions to minimize electrical noise, which can lead to the optimization of the electrical signals in a PEDOT:PSS film for the bio-sensing applications.

Chapter 5

Abstract in Korean

초록

유체흐름 및 전기적 노이즈 제어를 통한 바이오센서 검지능 향상법에 대한 연구

위험 바이러스의 조기경보, 식료품 품질검사, 수질오염 검사, 생화학 테러 방지 등, 다양한 분야에서 바이오 검지 시스템의 중요성이 높아지고 있다. 특히, 최근 나노물질을 기반으로 하는 여러 바이오 검지시스템이 개발되면서, 기존의 바이오 검지 시스템에서는 얻을 수 없었던 고성능의 검지시스템 제작이 가능하게 되었다. 하지만 이러한 시스템 조차 물질 자체의 고유한 물리적 특성 한계로 인하여 반응속도, 검지감도 등의 한계가 여전히 존재하였다. 본 연구에서는 기존 바이오 검지시스템의 이러한 한계를 극복하고 성능을 향상시키기 위한 방법에 대하여 논의하였다.

먼저, 검지용액의 측면유속을 제어함으로써 바이오 검지시스템의 특성을 향상시키는 전략에 대하여 연구를 진행하

였다. 측면유속 제어 전략은 바이오센서의 표면에 검지용액의 측면흐름을 발생시켜, 기존의 물질확산 방식의 바이오센서보다 검지속도/검지감도/선택성 등의 센서 특성을 향상시키려는 전략이다. 본 전략에서는 회전기판에 목표물질을 검지할 수 있는 바이오센서를 회전기판의 바깥 부분에 부착하고, 기판을 회전시켜 바이오센서 표면에서 검지용액의 측면흐름을 발생시켰다. 실험결과, 이러한 바이오센서 주변에서의 물질흐름 제어는 바이오센서의 반응속도 및 반응감도 향상, 비선택적 반응량 감소, 극한환경에서의 검지특성 향상 등 바이오센서의 전반적인 특성을 향상시킬 수 있음을 증명하였다.

바이오 검지시스템의 성능향상을 위한 또 다른 연구로, 바이오센서의 검지한계를 결정하는 전기적 잡음에 대한 연구를 진행하였다. 본 연구에서는 최근 바이오센서의 재료로 많이 사용되고 있는 PEDOT:PSS 전도성 폴리머에 대해 진행되었으며, 전기적 잡음 분석이 가능한 원자힘현미경을 통해 나노미터 범위의 매우 작은 지역에서의 전류 및 전기잡음 분석을 진행하였다. 실험결과, PEDOT:PSS 박막의 전기적 잡음을 발생시키는 잡음원들이 박막 전체에 걸쳐 불균일하게 분포되어 있었으며, 이 잡음원들은 외부 인가전압에 따라 잡음원의 밀도가 비이상적으로 변화하는 현상을 보였다. 특히 이러한 전기적 잡음원 밀도의 비이상적 변화거동은 PEDOT:PSS 박막의 전류특성과 매우 밀접하게 연관되어 있음을 확인하였다. 본 연구결과를 통해, PEDOT:PSS 박막에서의 전기적 잡음원을 최소로 하고, 전기 신호를 최적화 할 수 있는 외부조건이 있음을 확인

하였으며, 이는 다양한 PEDOT:PSS 박막 및 전기기반의 바이오 검지 시스템에 적용 가능할 것으로 기대된다.

주요어: 바이오센서, 측면 유속, 결합력, 비선택적 흡착, 스캐닝 노이즈 현미경, 전기적 잡음, 전하 트랩

학번: 2012-30109

Appendix

A. Simulation of Cell Reynolds Number

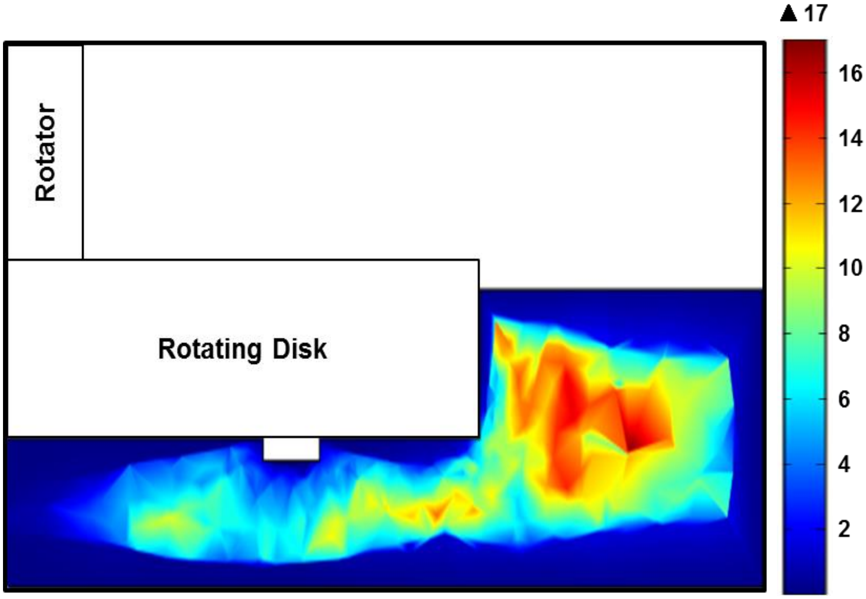

Figure A1. Simulation of Cell Reynolds Number.

Cell Reynold number (Cell *Re*) has been often utilized for the estimation of turbulent flows. The number indicates local Reynold number based on the velocity of flow in each cell. In this case, the each cell was assumed as a pipe, and we can compare the calculated number with previous reported *Re*. Generally, turbulent flows are generated if *Re* is higher than 2000 in a pipe. Our results show much lower *Re* than previous works, which indicates the laminar flows are dominant in the system.

B. Simulation of Lateral Flows on Sensing Substrates

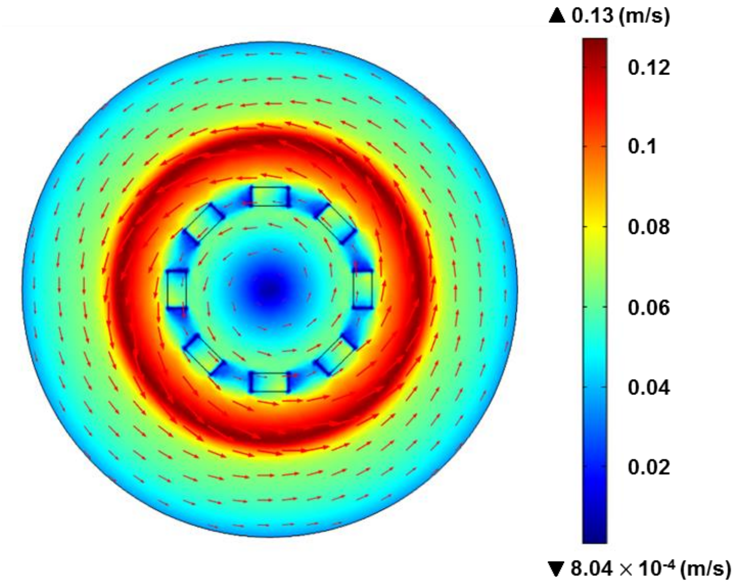

Figure A2. Simulation of Lateral Flows on Sensing Substrates.

The lateral flows on the sensing substrates were also simulated. The rotation speed of the disk was fixed with 150 rpm. The result shows the increase of lateral flow speeds from a center to the edge region of the disk, and the lateral flow speeds decrease again to a chamber wall. The highest flow speed is observed at the edge of the disk. Furthermore, the simulation shows no turbulent flows in the reaction chamber.

Acknoledgement

우선 오랜 시간 동안 많은 가르침을 주신 홍승훈 교수님께 깊은 감사 드립니다. 교수님으로부터 이뤄 말할 수 없을 만큼 많은 것들을 배웠지만, 몸소 보여주셨던 논리적인 사고와 열정적인 모습은 앞으로도 제 삶의 큰 교훈이 되어 저 자신을 옳은 방향으로 이끌어 줄 것임을 믿어 의심치 않습니다. 항상 많은 도움을 주셨던 교수님께 진심으로 감사 드립니다.

연구실에서 힘들었던 순간들이 힘든지 모르게 해주셨던 많은 분들께 감사 드립니다. 후배사랑 1등 성영누나, 실험 멘토 광이형, 멘탈 멘토 선이형, 무슨 일이든 쉽게 해내는 태경이형, 생각치도 못할 때 감사하게 만드는 병주형, 유일하게 술 사주던 주형이형, 항상 반가운 동희형, 게임빼고 뭐든 잘하는 형우, 나한테만 반말하는 영모, 정의 할 수 없는 주훈씨, 똑쟁이 혜준씨, 아우라 있는 동준이, 중국어 엄청 잘하는 세홍씨, 항상 듬직하신 강병수 박사님, 큰 꿈 품은 박은진 박사님, Beautiful Maaroof 박사님, 울보 Thao 박사님, 인도 최고미남 Shekhar 박사님. 함께 해서 항상 즐겁고 감사했습니다.

연구실 우상 이병양 선배님, 멀리서도 항상 후배들 챙겨주시는 임지운 선배님, 슈퍼맘 변경은 선배님, 밝은 미소 백구연 박사님, 시원시원한 민백 형님. 선배님들 덕분에 연구실이 항상 자랑스러웠습니다.

처음 연구실 왔을 때부터 가장 오랜 시간 함께 해준 진희누나, 대산이, 덕형이, 정수. 좋은 추억 만들어줘서 고맙고, 즐거웠다! 20년 지기 같은 하늘이, 아니~ 명재, 최고 부지런쟁이 민주, 조용히 잘해나가는 나래, 속세에 통달한 영탁이, 내 동생 Viet, 비드 마스터 중현이, 연구실 살림꾼 진영이, 명품 목소리 인경이형, AFM 차기 주자 지혜. 모두들 감사합니다!

기댈 곳 없는 서울에서 마음의 안식처였던 종하형, 성언, 근수, 용석, 진형, 명환, 진용, 홍식, 장원. 진심으로 감사합니다.

내 친구 동규, 동욱, 동환, 용민, 일혁, 한얼. 항상 보고 싶다.

진심으로 내 걱정해주는 용환이 정말 고맙다.

마지막으로 가장 소중한, 아무 말 없이 항상 제 뒤를 지켜주신 사랑하는 아버지, 어머니. 앞으로는 제가 지켜드리겠습니다. 여린 마음에 맘고생 많았던 내 아내 주연아, 정말 고생했어. 언제나 내가 지켜줄께 사랑해. 내가 걱정할까 조용히 집안 챙겨준 너무 고마운 누나. 우리 집 비타민 꿈 많은 막내 현미. 마음으로는 항상 챙겨주고 싶은 1등 신랑감 처남. 부족한 사위에게 항상 베풀어주시는 장인어른, 장모님 감사하고 사랑합니다. 사랑하는 우리 가족 항상 행복하고 즐거울 수 있도록 큰 울타리가 되겠습니다. 고맙고 사랑합니다.

2019. 01. 22.

조동국 올림